NOVEMBER 2, 2017

SPELEOTHEMS AND ISOTOPES

A LATE HOLOCENE PALEO-CLIMATOLOGICAL RECONSTRUCTION USING A STALAGMITE FROM RODRIGUES ISLAND

FRAMBACH, M. (MARISSA)

Universiteit Utrecht
Faculty of Geosciences

MAX-PLANCK-INSTITUT FÜR CHEMIE

NIOZ

Contents

Abstract

According to the IPCC report of 2013, anthropogenic warming has increased the Earth's global energy inventory since the industrial revolution. 93% of this warming is taken up and locked in the oceans. However, heat uptake is not equally distributed over the oceans. Sea Surface Temperatures (SST) in the South-Central Indian Ocean are shown to have a larger increase than the global average SST increase. Interannual SST variability in the Indian Ocean is known to be the result of the interplay between the East Asian monsoon, El Niño–Southern Oscillation (ENSO) and the Indian Ocean Dipole (IOD). Correlation between the Pacific Decadal Oscillation (PDO) and ENSO suggests that intercorrelation between climatological drivers complicates regional SST patterns. How the climatological drivers developed over time and what the trend will be in the future is not known. The precession-driven shift of the Intertropical Convergence Zone (ITCZ) in combination with an obliquity maximum led to the Holocene Climatic Optimum (HCO) around 9000-5000 years ago. This period was characterized with warmer summers in the Northern Hemisphere and colder on the Southern Hemisphere. The African climate is driven by climate variability on the Northern Hemisphere; Asian monsoon strengthening led to the African Humid Period (AHP). After the HCO, the Southeast African region was characterized by general cooling and drying. Speleothems are known to be an excellent archive of the past, able of reconstructing precipitation and temperature variability. Rodrigues Island is located in the Southwestern Indian Ocean. The location of the island is optimal for deciphering the interplay between modulating climate phenomena and interconnection between the shifting positions of the ITCZ and the Mascarene High in the Indian Ocean. In this thesis, a 1550-year isotope record derived from a stalagmite from Rodrigues Island is presented from the Late Holocene (2700-1200 BP). An oxygen and carbon isotope record in combination with XRF data and clumped isotopes led to a paleo-climatological reconstruction. Temperature was reconstructed with both clumped isotopes and fluid inclusion data from Spliethoff [2015]. The record showed increasing aridity over the whole record with stable temperatures, agreeing with the global trend and the subtropical climate. Zonally shifting high-pressure areas in the Indian Ocean possibly caused rainfall variability in the region. A significant increase in humidity occurred between 1375-1275 BP and was linked to an increase in El Niño intensity, forcing the system in a positive Indian Ocean Dipole (IOD) state. Wavelet analysis showed a 300-year cyclicity of these decadal-scale transitions to a positive IOD, agreeing with other research on Mauritius by De Boer et al. [2014]. Due to global warming, increased heat uptake by the Indian Ocean is expected in the future, causing further desiccation of the Rodrigues Island area.

Introduction

1.1. General introduction

The South-Central Indian Ocean is known to be a focal point of heat uptake, leading to a larger increase in its sea surface temperatures (SST's) than the average global SST increase (Lee et al., 2015; Roxy et al., 2014). Recently, this increased heat uptake has been explained by an asymmetric response of the Indian Ocean to El Niño-Southern Oscillation (ENSO) variability; El Niño conditions cause anomalously warm SST's in the Western and Central Indian Ocean, while La Niña's do not cause anomalously cool SST's in that region (Roxy et al., 2014). This effect will be enhanced by the increased frequency of El Niño events in a world that is warming by increased greenhouse gas output (Cai et al., 2014). It is unknown what the role of the main coupled air-sea interaction of the Indian Ocean, that is the Indian Ocean Dipole (IOD), is for this Western and Central Indian Ocean warming.

The recent warming of the Indian Ocean can be ascribed to the buildup of warmer waters due to the long-lasting La Niña events with a lacking balancing El Niño event (Baudoin et al., 2017; Cai et al., 2014; Lee et al., 2015). The increased warming of the South-Central Indian Ocean is thought to weaken convective atmospheric flow to Southeast Africa, resulting in drought and famine in that area (Baudoin et al., 2017; Funk et al., 2008). This should simultaneously result in higher precipitation in the South-Central Indian Ocean. The current most accepted hypothesis for the increased heat uptake in the Indian Ocean is the recent intensification in the interplay between modulating climate phenomena in the Indian and Pacific Ocean (Abram et al., 2008).

To understand the relation and future response of the system and the intercorrelating climatological phenomena, research is needed, especially on the Southern Hemisphere (Marcott et al., 2013).

1.2. Climatology

The Indian Ocean climate is primary dependent on the seasonally shifting Intertropical Convergence Zone (ITCZ) (figure 1). The ITCZ is a wind convergence zone, characterized by relatively heavy precipitation. This zone shifts latitudinally towards the warmest SST. Latitudinal SST variability is driven by yearly changes in the angle of incoming solar radiation due to the tilt of the Earth's axes, also known as seasonality (Schneider et al., 2014). The location of the ITCZ determines the onset and duration of global rain patterns and the monsoonal season(s) (Fleitmann et al., 2003). Its northern latitudinal maximum in July and southern latitudinal maximum in January (figure 1). Rainfall patterns in the (sub)tropics correlate with the latitudinal migration of the ITCZ (Schneider et al., 2014).

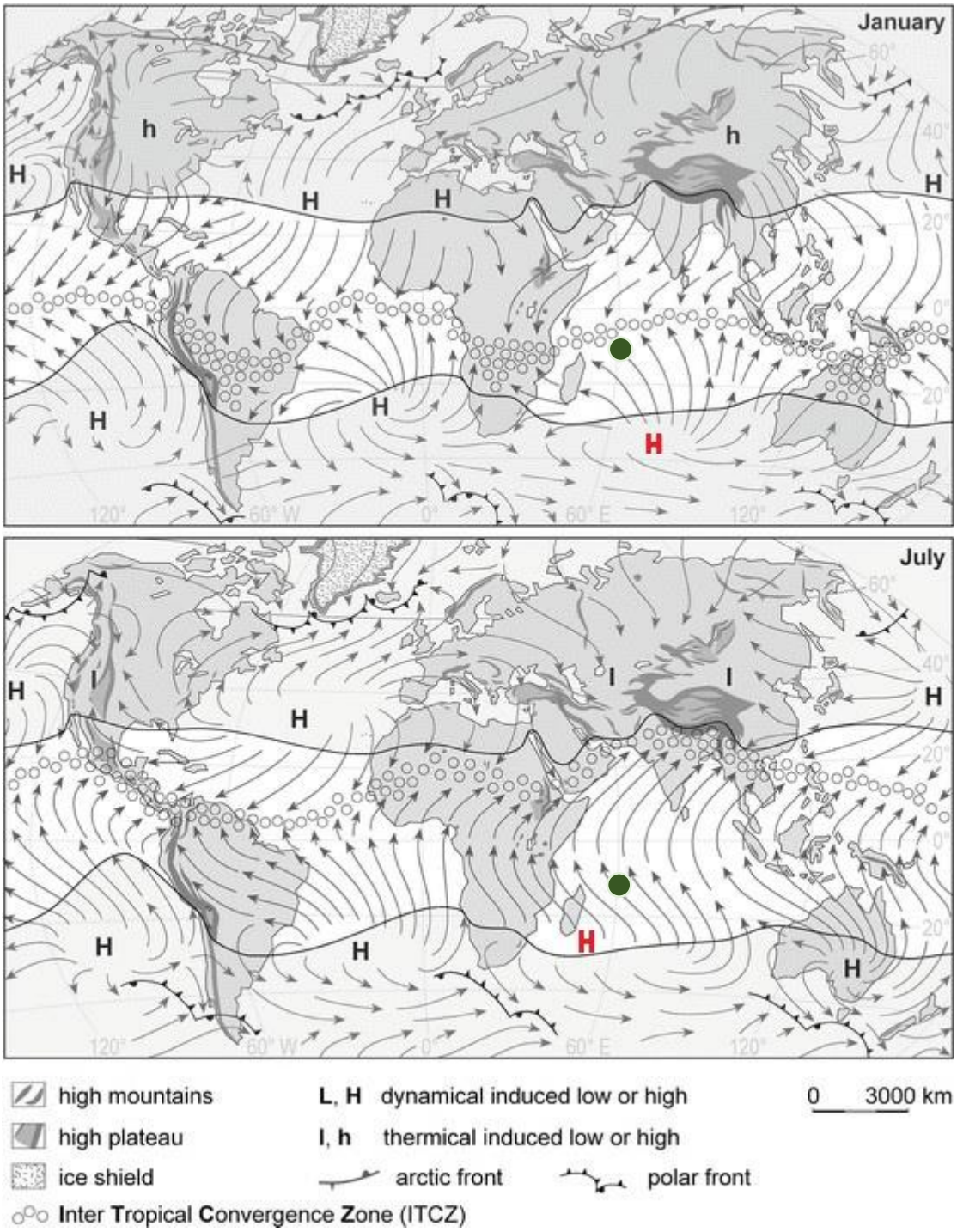

Figure 1. The migration of the ITCZ with its two maxima in January (top figure) and July (bottom figure). The location of Rodrigues Island is indicated as a green dot. The Mascarene high pressure area is indicated with a red H. Note the northward movement of the ITCZ in July. Dominant wind patterns (surficial) are illustrated as arrows. Modified from Richter [2001]. The solid fixed lines in the figure are the borders between the tropical and extratropical climates as defined by Troll (1950). Note that topography and position of continents influence atmospheric circulation.

Generally, ocean circulation in the Indian Ocean subtropical gyre occurs in two gyres: A Northern and Southern gyre (Lutjeharms, 2006; figure 2a). The South Equatorial Current (SEC) brings warm water and moist air from Indonesia to Africa and splits the Indian Ocean gyre in two. Water mass exchange between the Pacific and Indian Ocean occurs mainly

through Indonesia, which is called the Indonesian Throughflow (ITF), transporting about 10-15 Sv (Linsley et al., 2010). Other inflow occurs from the southern Indian Ocean, through the Antarctic Circumpolar Current (ACC) and the Red Sea. The Agulhas Current is the most important outflow transporting water masses from the Indian Ocean along the coastline of South-Africa to the Atlantic Ocean reaching up to 70 Sv, making it the most important western boundary current (Lutjeharms, 2006; Bryden et al., 2005, figure 2b). The ITF is the link between the IOD and ENSO causing SST anomalies in the Indian Ocean (Newman et al., 2003; Wang et al., 2014).

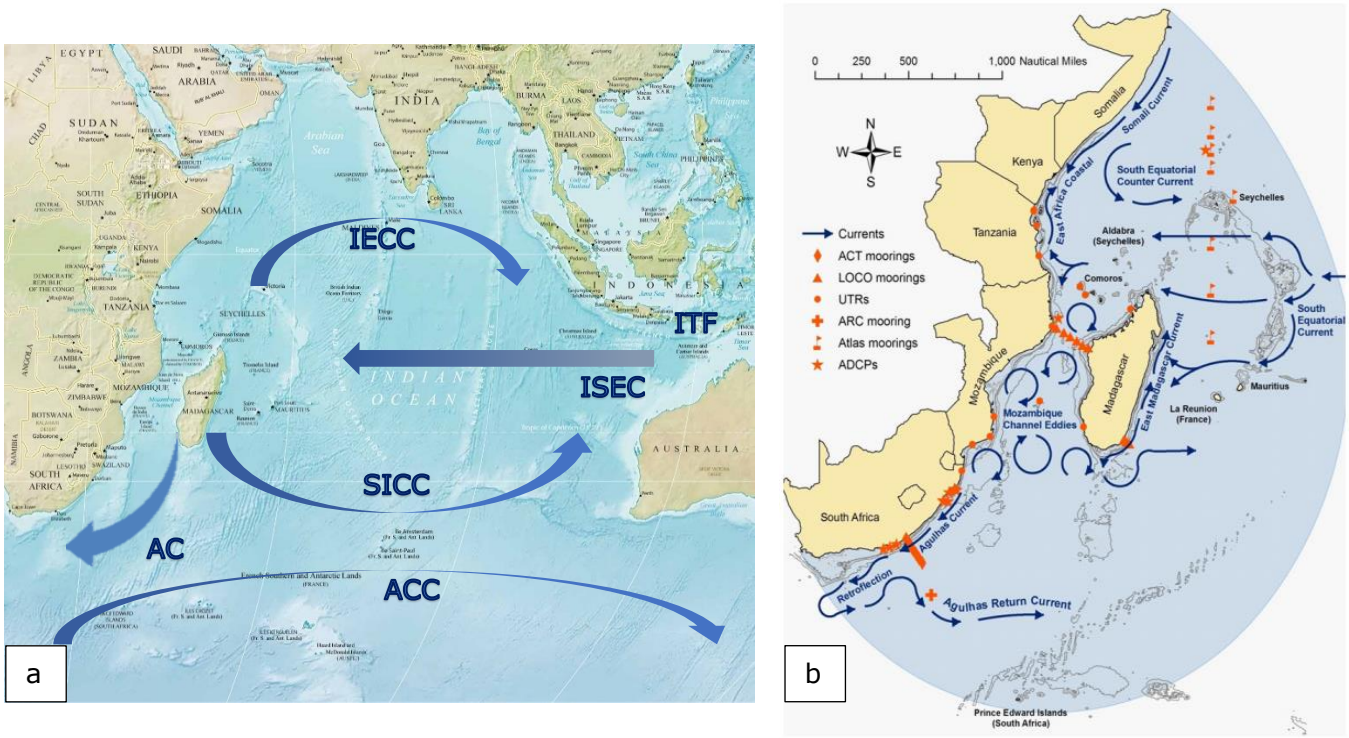

Figure 2. Figure 2a gives an overview of the Indian Ocean circulation; subtropical gyre split by the Indian South Equatorial Current (ISEC) bringing water westward. The Indian Equatorial Counter Current (IECC) and South Indian Counter Current (SICC) bring water eastward. Inflow occurss through the Indonesian Throughflow (ITF) and Antarctic Counter Current (ACC). Outflow occurs through the Agulhas Current (AC). Figure 2b shows the submesoscale ocean circulation around Madagascar as presented by Lutjeharms and Bornman [2010].

1.3. Indian Ocean Dipole

Changes in the SST of the Indian Ocean correlate with changes in the strength of the trade winds and/or southern Westerlies. 12% of the changes in SST can be ascribed to the Indian Ocean Dipole (IOD) (Saji, 1999). There are three phases of IOD: positive, negative and neutral. In neutral phase, air rises around Indonesia and sinks in the western Indian Ocean, completing the cycle with westerly winds blowing along the equator. In case of a positive (negative) IOD event anomalous warmer (colder) temperatures are visible in the (south)western Indian Ocean and colder (warmer) in the Southeastern Indian Ocean, creating a dipole structure. Every phase occurs every 3-5 years. Positive or negative phases occur in autumn/winter and return to neutral around the end of spring when the northern Australian

monsoon arrives (Behera et al., 2006; Saji, 1999). With the east-west (west-east) temperature anomaly gradient, westward (eastward) shift of the Walker Cell by weakened (intensified) westerly winds causes an increase (decrease) in upwelling in the eastern Indian Ocean, leading to an increase (decrease) in productivity in the Sumatran waters, an increase (decrease) in precipitation in western Indonesia, a decrease (increase) in precipitation in Australia and drought in Africa (Behera et al., 2006; Kwiatkowski, et al., 2015).

Climatological models suggest that internal variability of SST in the Indian Ocean is initiated by a(n) decrease (increase) in the thermocline depth during El Niño (La Niña). Thus, the ITF decreases (increases) during El Niño (La Niña) events; since the ITF transports warmer Pacific waters into the Indian ocean, anomalous lower (higher) temperatures are found in the eastern Indian Ocean, the positive (negative) phase of IOD. These two climate phenomena have had global climatological impact with records indicating the extent over the whole Holocene epoch (Abram et al., 2007; De Boer et al., 2014).

Not only the position, also the intensity of the ITCZ is altered by the IOD. During a positive IOD, the ITCZ weakens and precipitation intensifies north of the ITCZ (Saji et al., 1999). Correlation between the main high-pressure area around the Mascarene Islands, the Mascarene High, short rainfall events in eastern Africa, the IOD and ENSO support the idea of changing location and intensity of the ITCZ (Baudoin et al., 2017; Manatsa et al., 2014). It is unclear if the Pacific Decadal Oscillation (PDO), which describes decadal cyclicity in SST in the Northern Pacific, is a dominant driver in this region (Mantua and Hare, 2002; Newman et al., 2003). However, correlation between the PDO and ENSO is acknowledged (Newman et al., 2003; Wang et al., 2014) influencing the Indian summer monsoon rainfall (Krishnan and Sugi, 2003).

1.4. Rodrigues Island

The location of the island is optimal for deciphering the interplay between modulating climate phenomena in the Indian Ocean since the islands paleo-archives are ideally located to directly reflect oceanographic and atmospheric changes due to its maritime climate and isolated location (figure 1 and 3).

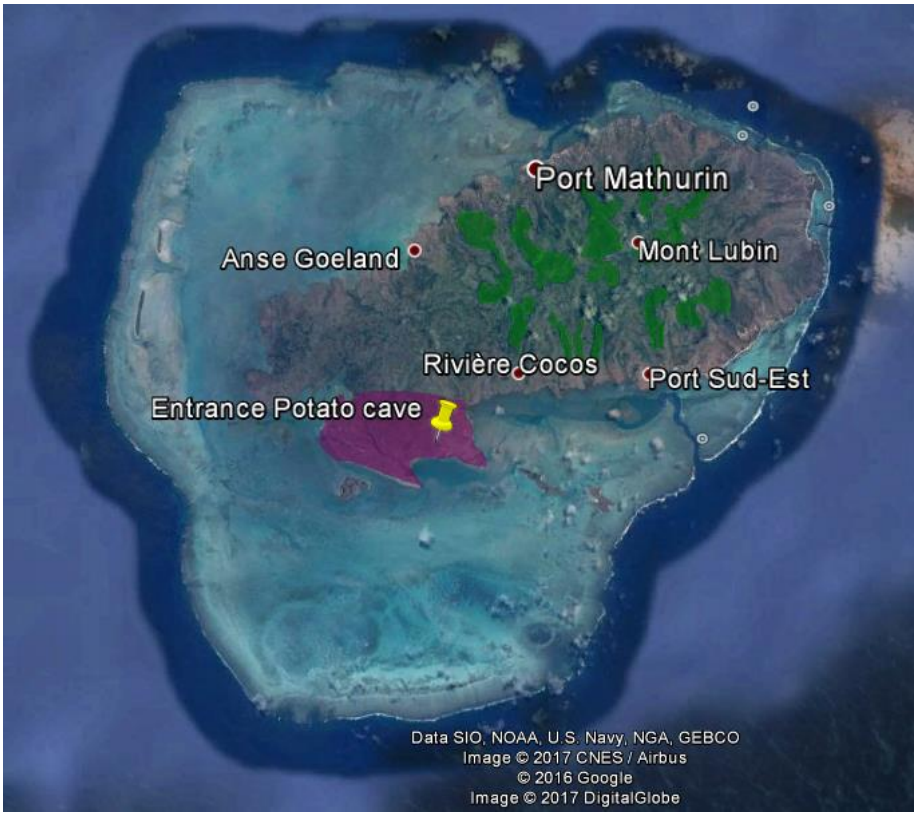

Figure 3. Rodrigues island including surrounding coral reefs and important cities (red dots, labelled). The entrance of the Potato cave (yellow point), the Caverne Potato area (purple) and patchy vegetation cover (green) are indicated. No (significant) vegetation cover around the Caverne Potato area is present. Image adjusted from Google Earth and Google Maps.

The long term annual precipitation and temperature over the period 1961-2007 is listed in figure 4. The wettest month is February, the driest months are September and October. The annual temperature variability lies between 20-30 °C. Highest temperatures are reached in January-March and the coldest around August, see figure 4. The island is located between the ITCZ and a high-pressure area called the Mascarene high (figure 1), resulting in prevailing trade winds with constant wind speed without seasonal/monthly variations and, according to Windfinder©, with an east/east-southeast direction (figure 4).

1.5. Stalagmites; paleo-archives

The isotopic composition of calcium carbonate ($CaCO_3$) in speleothems is known to be an excellent archive of past climatic and environmental conditions like temperature and relative humidity (Fleitmann et al., 2003; Lachniet, 2009; McDermott, 2004). Both the carbon (^{13}C) and oxygen (^{18}O) isotopes include more than one variable in their isotope value (Bar-Matthews et al., 1996; Lauritzen and Lundberg, 1999). The $\delta^{18}O$ signal reflects cave temperature and the isotopic composition of formation water or so called meteoric water (Feng et al., 2014; Grant et al., 2012; Ravelo and Hillaire-Marcel, 2007). The isotopic content of meteoric water can be determined by measuring the isotopic composition of fluid inclusions in the stalagmite (Eiler, 2011). The $\delta^{13}C$ value in the stalagmite has bedrock, atmospheric

and gas sources (Dorale and Liu, 2009; Lauritzen and Lundberg, 1999). Additionally, several incorporated trace elements might reflect trends in paleo-environmental conditions and can eventually pinpoint different signals found in the isotope value (Fairchild and Treble, 2009; Folk and Land, 1975; Verheyden, 2004).

a

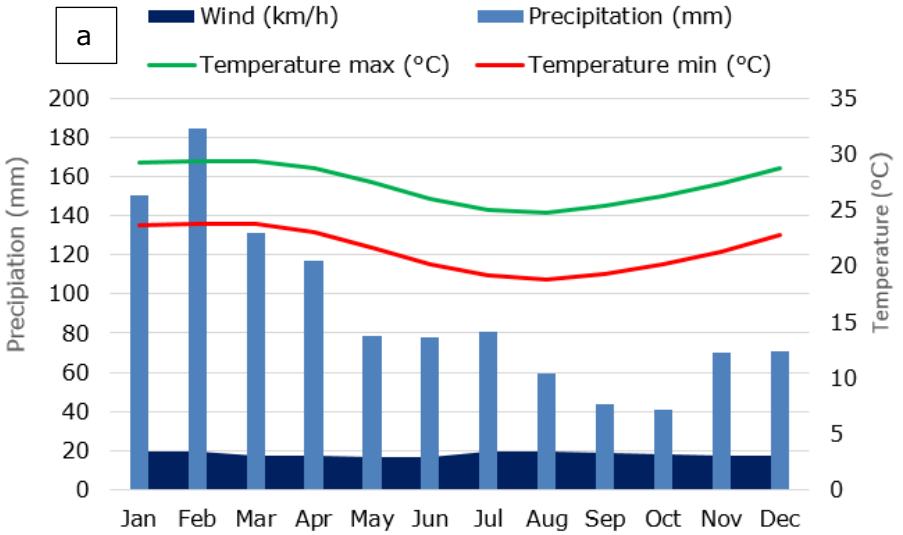

b

Mean precipitation (mm)		
Annual	*Summer*	*Winter*
1116	729	392
100%	65%	35%

Temperature (°C)		
Annual	*Summer*	*Winter*
24.1	25.9	22.3

Figure 4. Monthly mean precipitation, wind speed and temperature of Rodrigues island. In figure 4a, precipitation and wind speed are shown on the right axis, whereas temperature is shown on the left axis. Exact values are listed in the table in figure 4b. Data derived from Mauritius Meteorological Services: http://metservice.intnet.mu/climate-services/climate-of-rodrigues-and-islands.php

1.6. Clumped isotopes

The clumped isotope thermometry focusses on the abundance of naturally occurring molecules with more than one rare isotope. In carbonates, rare isotopes can either be oxygen (^{18}O) or carbon (^{13}C). This method assumes homogeneous isotope exchange equilibrium during deposition and can therefore not be executed after failing the Hendy test (Eiler, 2011; Hendy, 1971). Elaboration on the Hendy test can be found in section 2.5. The abundance of the ^{18}O-^{13}C bonds correlates with the temperature component in the isotope signal in speleothems since it is independent of the isotopic composition of meteoric waters from which the carbonate minerals originated (Douglas et al., 2014; Eiler, 2011; Kele et al., 2015; Meckler et al., 2015). When combining the isotopic data with the clumped isotopes data, one can differentiate between the temperature and precipitation component of the found signals in the trend. If temperatures derived from clumped isotopes are relatively stable, the dominant signal is humidity variability. When the signals are split, the trends can be extrapolated to paleo-environmental variability (van Breukelen, 2009).

1.7. Aim of this thesis

The aim of this thesis is to explore the use of speleothems to extend the knowledge on interannual climatological variability in the subtropical Indian Ocean in the Late Holocene and to help unravel the relation between the intercorrelating (interannual) oscillating climatological drivers of the convective ocean circulation in the South-Central Indian Ocean.

In this thesis, a speleothem proxy is used to produce a high-resolution $\delta^{18}O$ and $\delta^{13}C$ isotope record. With these results, trends in paleotemperatures and paleohumidity will be reconstructed. Clumped isotope thermometry will make a distinction between the humidity and temperature signal in the isotope value. The record will be compared with other speleothem data from the cave and with prior research in the Southeastern Indian Ocean. Comparison with these existing data sets will give an overview of the climatological changes in the Holocene in this area. The main research question of this thesis is:

Which climatological drivers were dominant in the Late Holocene causing SST variability in the subtropical Indian Ocean?

Additional sub-questions to aid the research question are:

- Which cyclicities are present and dominant in the speleothem record?
- How are the cyclicities interconnected in the speleothem record?
- What is the regional and global pattern when the data is extrapolated?

Materials and methods

2.1. Location description

Rodrigues Island is located in the Southwestern Indian Ocean about 1500 km east of Madagascar with coordinates 19°42'S and 63°24'E (figure 1). It lies in the Mascarene Basin and forms with Reunion and Mauritius Island the Mascarene Archipelago. The surface area of the island covers about 108 km^2 and the highest point is reached at 396 m. The island foundation consists mostly of igneous rock and rose from the sea at about 1.5 million years ago, due to volcanic activity around the meeting point of three tectonic plates; namely the African, Australian and Antarctic plate (Cheke and Hume, 2010). The island is almost continuously encircled with coral reef with a small southeast river outlet. In the southwestern part, several karst features mark the presence of the limestone formation underneath the surface; about 3 km^2 of the surface between Plaine-Corail and Baie-Topaze is covered by limestone rock (figure 3). The limestones on the island are eolian calcarenites and are formed on top of the basalt foundation of the island. The southwestern location of the eolianites can be explained by the present dominant wind direction and ocean circulation (Burney et al., 2015; Lace and Mylroie, 2013; Middleton and Burney, 2016).

The limestone formation includes over 30 surveyed dissolution caves. Among these is the most extensive cave known in the Republic of Mauritius, the Caverne Patate or in English, the "potato" cave. This chained cave system reaches a length of 1,040 meters and has its entrance at coordinates S19°45.492' E63°23.191' (figure 3). Part of the Caverne Patate system is the "Cave aux Crabes" or Caverne de la Vierge, shortly "La Vierge". The cave is a "fossil stream cave" since it is the remnant of a former flowing water body (Middleton and Burney, 2016).

The first inhabitants arrived in 1691 (Gade, 1985). Sharp population increase led to a population of 42,058 in 2015 (Cassimally, 2015). It was a British colony until declaration of independence in 1962. (Stuart et al., 1990). Human impact led to deforestation, cultivation and introduction of invasive species. Altering of the islands hydrology and biodiversity led to environmental degradation and fragmentation (Gade, 1985). Currently Rodrigues has three conservation areas, covering about 0.58 km^2 (WWF and IUCN, 1994).

The stalagmite was harvested during an expedition, led by Hubert Vonhof, 4 years ago (2013). A slab of 0.5 cm was sawn out of the center of the stalagmite. The surface was scoured with sandpaper, using increasingly finer grit sizes: from 600 up to 2000 according to the ISO/FEPA grit designation. The centered slab was used for all measurements. The cave air humidity was about 100% (Rijsdijk et al., 2011). The average cave air temperature was 25.5 °C which is higher compared to an average 20-25 °C outside temperature (Spliethoff, 2015; Rijsdijk et al., 2011; graph 1).

2.2. Preparing for sampling

2.2.1. XRF

Several scans and pictures from the stalagmite were taken by an Avaatech scanner before choosing a sample drill path. This machine is equipped with an XRF-scanner and can make high resolution line-scan pictures, both under visible and ultraviolet (UV) light. For a precise description of the machine's specifications, one can visit http://www.avaatech.com. With the XRF-scan, counts of all elements over a cross-section can reveal possible, color-correlated, trends in (trace)elements (Frisia et al., 2005; Dendurand et al., 2011). The stalagmite was exposed to 10 kV and 30 kV X-rays. Spectral analysis will give insight into possible trends and cyclicity within the data. The counts measured should be 10 times above the standard deviation for the signal to be significant to the background noise.

2.2.2. UV-radiation

Ultraviolet radiation on carbonates is known to show luminescent banding in both corals and stalagmites up to annual scale (Baker et al., 1993). Trends in the UV-radiation cross-section was quantified according to Hunter's L, a, b color space principle (1942). This principle states that all colors can be divided into two color dimensions, a and b. The lightness L^*, where $L^*=0$ at its darkest color (black) and $L^*=100$ at its brightest color (white), gives the luminescence. The luminescence is caused by incorporation of organic acids derived from the overlying soil (Baker, 1996) The stalagmite was exposed to UV radiation with a range of different exposure times. The best setting was found at an exposure time of 20 milliseconds through an f/2.8 aperture.

2.2.3. X-ray radiation

Lastly, before setting out the sample path, the stalagmite was exposed under X-ray radiation. Internal density variability can reveal hidden growth history and detailed structures (Frisia, 1996). The best setting was an exposure of 50 kV for 120 seconds.

2.3. MicroMill sampling

Samples were drilled at the NIOZ institute, located on Texel Island, the Netherlands. A MicroMill with a 1 µm drilling precision was used. MicroMill sampling took place perpendicular with respect to the growth rings of the stalagmite in the center of the sample at a 500 µm interval. The path was shifted with the varying center of the growth bands. For the exact drilling locations, see figure 6. To prevent contamination of the sample by drilling through several layers, samples were drilled with a cut width of 50 µm. For the same reason, the drilling depth was set at 50 µm as well. Samples were drilled in 2000 µm long lines along the growth bands. The drilling speed was set at a constant pace of 15 µm/s.

Two sets of both 6 lines of 2000 µm were drilled to test the isotopic equilibrium during speleothem formation. To see if there is any difference between the different opacity of the layers, the tests are set in a milky and in a transparent layer. If isotopic equilibrium during formation is not reached, the stalagmite cannot be used for isotopic analysis.

2.4. Dating

Dating of speleothems occurs usually through U/Th dating. Uranium can be incorporated into the crystalline structure due to its solubility, while thorium is usually insoluble. Secular equilibrium is hereby excluded and the radioactive clock is reset. However, when initial thorium is not equal to zero, it will result in overestimation of age (Frisia et al., 2002).
The stalagmite was dated with U/Th at the two different points in the center of the stalagmite. The ratio was measured using inductively coupled plasma-quadrupole mass spectrometry (ICP-QMS), a method proved to be able to repetitive age measurement and precise numbers (Douville et al., 2010; Genty et al., 2003; Mallick et al., 2002). Although the stalagmite was harvested under an active drip, the age of the top is 1206 ±162 years BP. The second measurement was 4.2 cm top-down and is 1764 ±100 years BP (for locations, see figure 6). From these two U/Th measurements, an age model was fitted to the isotope records.

2.5. Isotopic equilibrium test

As the choice of equilibrium fractionation factor is critical when calculating temperature (McDermott et al., 2006), the reliability of the results was tested by applying the Hendy test (Hendy, 1971). There are two criteria to the test: 1) Isotopic equilibrium should be maintained over a single growth layer; when there is no equilibrium at deposition, the isotope value will enrich away from the apex due to kinetic fractionation. If values remain similar over the growth band, $^{18}O/^{16}O$ variations are caused by climatic variations only. 2) There is no correlation between $\delta^{13}C$ and $\delta^{18}O$, because they are both affected by climate differently. A discussion about the Hendy test can be found in section 4.1.

2.6. Isotope analysis $\delta^{13}C$ and $\delta^{18}O$

Isotope measurements of the La Vierge stalagmite were performed at the Max Planc institute, located in Mainz, Germany. The carbon and oxygen isotope values were measured following a method set up by Breitenbach and Bernasconi [2011]; the sample was treated by a GASBENCH preparation device, after which the carbon and oxygen isotope value was measured by a Thermo Delta V mass spectrometer (figure 5). Each sample had a typical mass between ~20-200 µg and was placed in 4 ml tubes. The samples were flushed with Helium gas to prevent bias via atmospheric contamination. The samples were digested with phosphoric acid (HPO_4^{-3}). Subsequently, the CO_2-He gas mixture is transported to the

GASBENCH in He-carrier gas. In the GASBENCH, water and other gaseous compounds are separated from the He-CO_2 mixture before sending it to the mass spectrometer. The mass of the released CO_2 was measured seven times by the mass spectrometer, which collects the ions with the Faraday collector. The average value of the seven amplitudes is the final value of the sample. The measured amplitudes decrease with number because of dilution of the sample. The isotope ratio mass spectrometer measures CO_2 with three different ion masses, 44, 45 and 46 mol/g: $^{12}C^{16}O^{16}O$, $^{13}C^{16}O^{16}O$ and $^{12}C^{18}O^{16}O$, respectively. Differences between the values will determine the $\delta^{13}C$ and $\delta^{18}O$. The isotope values are given as $\delta^{13}C$ and $\delta^{18}O$ relative to the V-PDB standard.

Two different series of standards were measured with different sample sizes. The standards were sampled from a uniform carbonate rock. For each run, the correction was calculated. The samples were plotted against amplitude and a logarithmic trend line was fitted. When filling in the amplitude in the equation, the correction was set per sample. The reproducibility of routinely analyzed lab $CaCO_3$ standards in this research was better than 0.1‰ (1 SD) for both $\delta^{13}C$ and $\delta^{18}O$. A logarithmic calibration curve is fitted through the measured data points, after which the right correction per measured amplitude can be applied. For calculating the temperature with the $\delta^{18}O$ (equation 1 as used by Lachniet [2009]), the time of precipitation and the initial $\delta^{18}O$ value of the formation water ($\delta^{18}O_{water}$) should be known. In the most precise case, fluid inclusions are used for paleo-$\delta^{18}O_{water}$ since fluid inclusions enclose old drip water in the cavities (e.g. Kluge et al., 2008; van Breukelen, 2009. The $\delta^{18}O_{water}$ is given in SMOW whereas the $\delta^{18}O_{carbonate}$ is given in VPDB (Feng et al., Spliethoff, 2015).

$$T = 15.75 - 4.3 \cdot (\delta^{18}O_{carbonate} - \delta^{18}O_{water}) + 0.14 \cdot (\delta^{18}O_{carbonate} - \delta^{18}O_{water})^2 \qquad \text{eq. 1}$$

After measuring the $\delta^{18}O_{carbonate}$, the average $\delta^{18}O_{water}$ from the thesis of Spliethoff [2015] was used. Although the speleothems are from the same cave, this will not give a true temperature. However, despite the differences, the calculated temperatures will get a general overview to validate the results from the clumped isotopes.

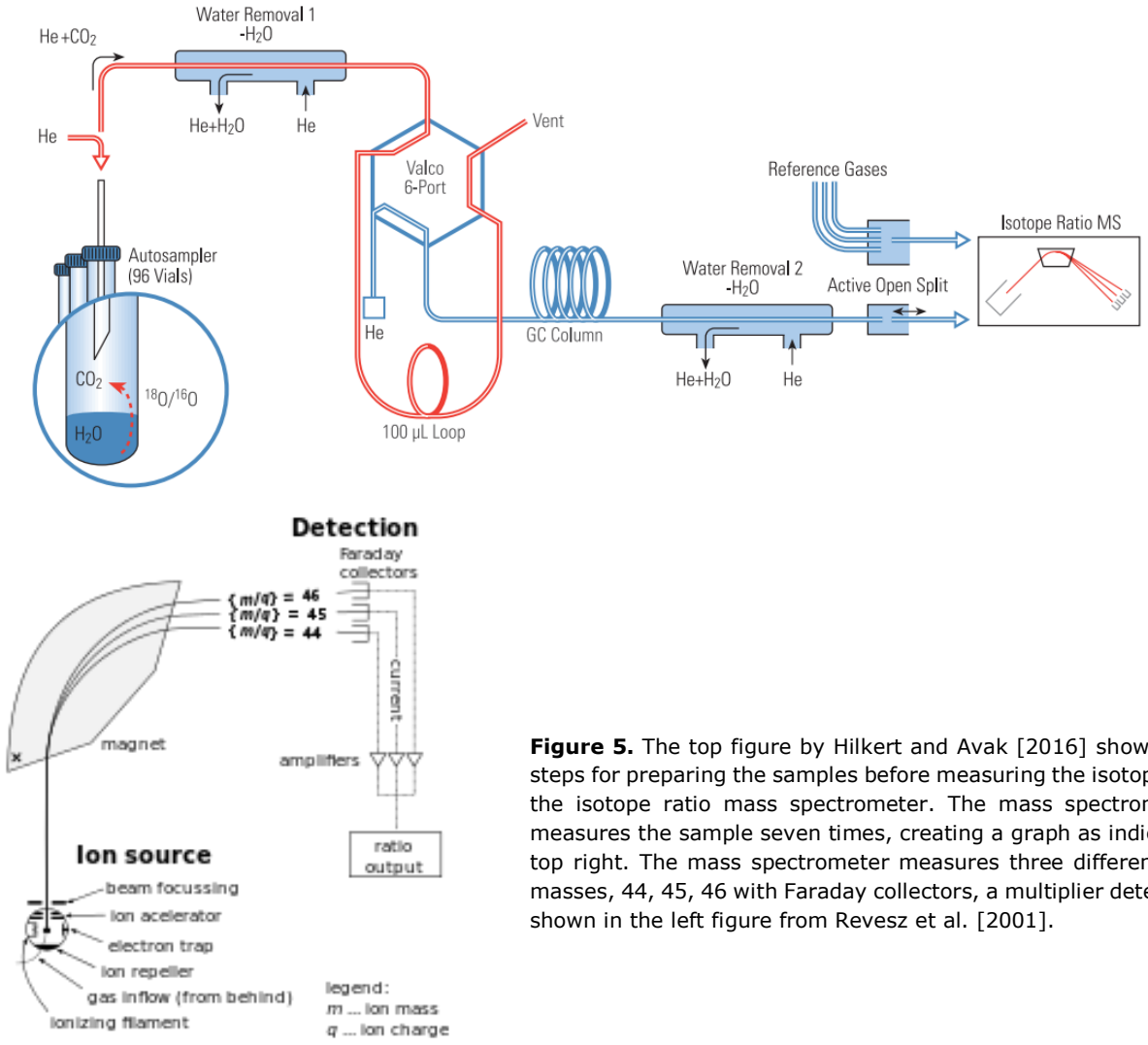

Figure 5. The top figure by Hilkert and Avak [2016] shows the steps for preparing the samples before measuring the isotopes in the isotope ratio mass spectrometer. The mass spectrometer measures the sample seven times, creating a graph as indicated top right. The mass spectrometer measures three different ion masses, 44, 45, 46 with Faraday collectors, a multiplier detector, shown in the left figure from Revesz et al. [2001].

Correction for biases related to the experimental setup include a correction for machine drift. As the machine executes its measurements, it deviates over time when the same sample sizes are measured. Therefore, the standards were measured randomly, not size-sorted. The second correction is due to differing sample size. The smaller the sample, the lower the amplitude measured by the machine. As the amplitude becomes smaller, the correction is bigger and thus the reliability lower. Therefore, a sample size too small (< 150 µg) should be avoided.

The effect of tube size on measured isotope value was investigated. Hypothetically, the smaller the tube size, the larger the ratio sample/volume. Thus, the measured amplitude would be higher. Using a smaller tube size would therefore work better for smaller samples. To test the hypothesis, samples were measured in two different tube sizes. I deviated between the tubes: uneven sample numbers in a different sized tube than the even numbers.

2.7. Frequency analyses

Correlations between isotopes is expressed with the correlation coefficient, R^2; when $R^2=1$, there is perfect correlation, whereas when $R^2=0$, there is no correlation. REDFIT spectral analysis will show if there is any cyclicity in the results (Schulz and Mudelsee, 2002). Additionally, Wavelet analysis will show cyclicity trends over the derived isotope records (Torrence and Compo, 1998). REDFIT spectral analysis and Wavelet analysis are executed with the program Paleontological Statistics, or for short PAST (Hammer et al., 2001). The program AnalySeries is used to execute Gaussian bandpass filters on the carbon and oxygen isotopes and selected element records (Paillard et al., 1996). Significant peaks from the REDFIT analysis will be used as filter. The filter should agree with the Nyquist frequency: the filter should be at least twice the sample resolution (Allen, 1977). Additionally, bandwidth or bandpass filter should fit over the data; overfitting as well as underfitting was avoided as it may lead to bias in the results after filtering (Allen, 1977).

2.8. Clumped isotopes (Δ_{47})

Clumped isotopes were measured at the GML laboratory, located in Utrecht, the Netherlands, following the method as described by Schmid and Bernasconi (2010). The method of the clumped isotopes resembles the method used in Mainz. However, because of the low concentration of Δ_{47}, high precision and different bias correction is critical during and after measurement.

The standard formula for calculating the temperature dependent mass-47 in permilles is given in equation 2, where R represents the ratio between the abundance to the most abundant carbonate isotopologue with mass-44.

$$\Delta_{47}(‰) = \left[\left(\frac{R^{\frac{47}{44}}}{R^{47}\ sample}\right) - \left(\frac{R^{\frac{46}{44}}}{R^{46}\ sample}\right) - \left(\frac{R^{\frac{45}{44}}}{R^{45}\ sample}\right)\right] \times 1000 \qquad \text{eq. 2}$$

Samples were treated with a Thermo Scientific Kiel IV carbonate device (more information https://goo.gl/YX5TSy), after which samples were transported into a Thermo Scientific MAT 253 isotope ratio mass spectrometer. Samples were dissolved in phosphoric acid ($H_3PO_4^{3-}$) at 70 °C . Water is quantitatively removed by flushing and trapped by the use of repetitive loops before the released CO_2 gas is ionized and measured over variable collectors to measure specific mass-to-charge ratio (*m/z*) of 44 up to 49 (figure 5). Precision in the measurements is obtained by measuring the CO_2 gas alternately against a CO_2 reference gas for six cycles. During each cycle, the beam intensity decreases and differs per Faraday collector (figure 5). The KIEL also corrects for "composition-specific artifacts causing the nonzero slope of the heated and equilibrated gas lines, which … was shown to be the result of negative backgrounds or 'pressure baseline' (PBL) signals in the Faraday cups of the

smaller ion beams, which are linearly related to the intensity of the major ion beam (m/z 44)" (Meckler et al., 2014). The total time for one Kiel run, including 22 samples and 6 aliquots of each standard, is about 36 hours. Every sample has a typical weight of 150-180 µg, which later is corrected for. In every run, four different standards were used to find the regression between temperature and Δ_{47}. A linear fit through the four standards can then determine paleo-temperature. The more standards and aliquots measured, the better the end-fit of the data and the more precise the paleotemperature. The standard deviation for the standards was typically 0.05 ‰.

The data was corrected for machine derived biases by standardization to create an absolute reference frame (Meckler et al., 2014). Other corrections are applied for acid digestion fractionation and whether there is an average standard offset by conducting regression. When the samples are normally distributed, the standard deviation gives the reliability and potential bias of the measurements; the lower the deviation, the higher the reliability of the results. Also, a different correction is applied for different types of carbonates (Perrin et al., 2014).

Four sample locations were determined. The four locations were chosen to compare the $\delta^{13}C$ and $\delta^{18}O$ variability. Every sample has a typical weight of 3-4 mg. For every sample that had to be measured, as many aliquots as possible were derived. After determining the temperature component, the variability can be explained. The isotope value of the sample will be determined as well. By comparing the results from the KIEL and the GASBENCH, the precision, accuracy and reliability of the two machines can be analyzed.

The Δ_{47} data was transposed to temperature using two different calibrations. The two calibrations have the same analytical setup but based on travertine and synthetic calcite respectively. First is the travertine calibration given by Kele et al. (2015) where the temperature is expressed in Kelvin. This equation can cover temperatures between 5 and 95 °C. Equation 3 gives the formula used in this paper including the standard deviations.

$$\Delta_{47}(‰) = \left(\frac{0.044 \cdot 10^6 \pm 0.005}{T^2}\right) + 0.205 \pm 0.047 \qquad \text{eq. 3}$$

The conversion from temperature in Kelvin (K) to temperature in Celsius (°C) is made by equation 4. The ± indicates the calibration error in the formula.

$$T\,(°C) = T\,(K) - 273.15 \qquad \text{eq. 4}$$

The second calibration method is based on synthetic calcite assessed at the University of Leeds as presented in the paper by Meckler et al [2014]. This method has a temperature range of 3.5 to 70 °C (equation 5).

$$\Delta_{47}(‰) = \left(\frac{0.044 \cdot 10^6 \pm 0.006}{T^2}\right) + 0.179 \pm 0.071 \qquad \text{eq. 5}$$

If the clumped isotopes measurements all would produce the same temperatures, variability within the isotope records would be caused by humidity. Temperatures derived from the stalagmite are expected to be around 25 °C, compared to the situation of today (figure 4). With the standard deviation (σ), sample bias can be evaluated and with that the internal validity of the temperature calculations. After temperatures are determined using the two different calibration methods, they are compared with the temperatures calculated with the formula by Lachniet [2014] (equation 1) and the $\delta^{18}O_{water}$ from Spliethoff [2015].

Before σ can be calculated, the results should first be proven to be normally distributed by making a QQ-plot for every sample. If all samples follow a straight line, the samples are normally distributed. The slope of the line is the standard deviation. A correlation coefficient (c) and Shapiro-Wilk test (W) was performed to calculate the validity of the results and the behavior of the samples. The null-hypothesis (H_0) of the Shapiro-Wilk test is that the samples are normally distributed; the hypothesis can be rejected if the samples are not normally distributed. The Shapiro-Wilk test gives a W and a p-value. The closer the W-value is to one, the closer the samples are to normal distribution. If the samples are normally distributed, the p-value gives the probability of getting the observed value of the test statistic. The smaller the p-value, the greater the evidence against the null-hypothesis. However, if samples are closely to each other, the samples are unlikely to have a large p-value. If sample size is small, the Shapiro-Wilk test may also give misleading results (Shapiro and Wilk, 1965). The tests were executed using RStudio version 1.0.143.

Results

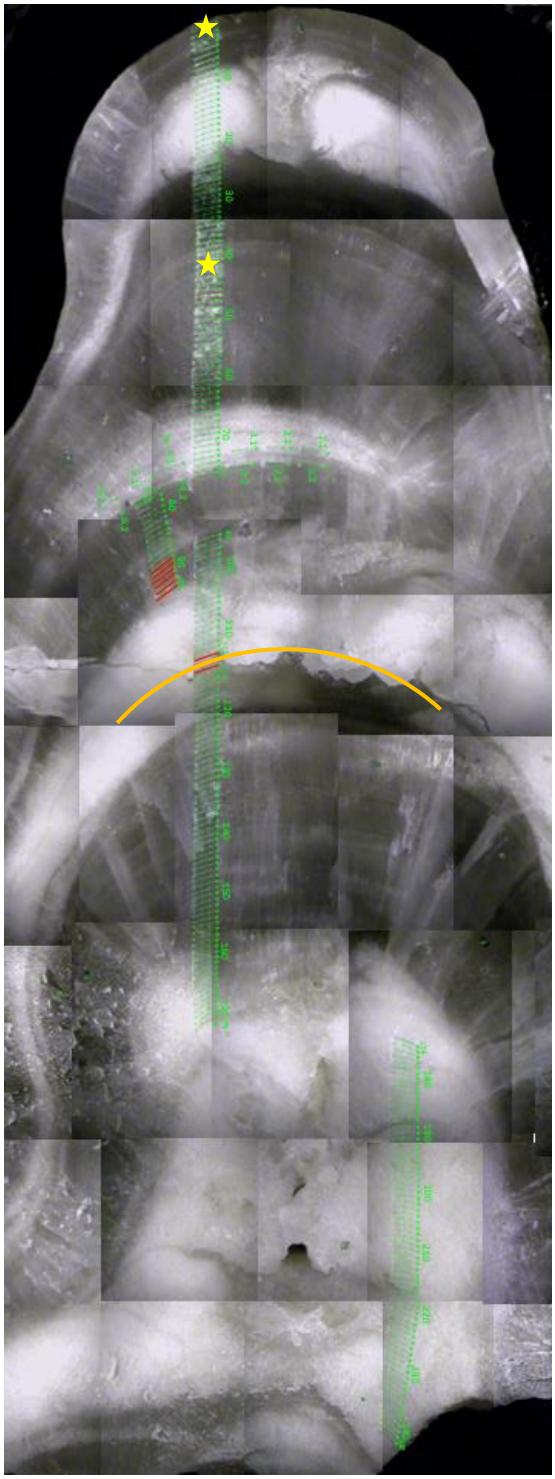

Figure 6. La Vierge stalagmite with all sample locations indicated as green lines. Red lines are unsampled. The orange arc indicates the fracture line on the second milky-white band.Black and white photos are taken with the MicroMill. Yellow stars indicate locations of U/Th measurements.

3.1. Stalagmite description

The La Vierge stalagmite is 121 millimeters long. The base of the stalagmite is 75 mm wide and it tapers towards the top where it flats out to approximately 30 mm. This shape is characteristic for a stalagmite, whereas stalactites have a more elongated shape (Short, 2005). Within the stalagmite, there is an alternation between milky-white, opaque layers and more transparent, clear layers. The color of the stalagmite suggests no or little intrusions of organic material. There are three distinct milky-white layers and a smaller one, only present in the core of the stalagmite. The base of the stalagmite (40-50 mm) consists of two milky-white opaque layered "shoulders" which can best be seen under X-ray (figure 7.2). The depression between the shoulders is a formation phenomenon caused by either the impact of falling drops (Bögli, 2012) or by dissolution occurring through partial periodic undersaturation of the drip water (Frisia, 2000). In the center of the base, several remnants of fluid inclusions and irregular growth bands are visible. It is therefore expected that isotopic analysis of the last samples will show more variations and will be less usable for analysis of paleoclimatology. The stalagmite has a fracture line on the second milky-white band, this section was not sampled (figure 6, orange arc); unsampled samples are marked red.

From the two data points (figure 6, yellow stars), a data model was extrapolated and the average growth rate is calculated. The average growth rate for this stalagmite was 42 mm/558 years = 0.075 mm/year. As the samples are taken every 0.5 mm, every sample overlaps about ~6.7 years. The average growth rates of stalagmites are 0.02-0.3 mm/year (McDermott et al., 2006; Genty et al., 2001). A growth rate of 0.075 mm/year value falls between this range, although relatively low.

The growth rate of a speleothem changes with temperature and drip water calcium content and to a lesser

extent, the drip rate (Lauritzen and Lundberg, 1999; Genty et al., 2001).

The certainty of the age model is highest when the sample lies close or in between the two U/Th data points (figure 6, yellow stars), and decreases towards the bottom of the stalagmite because of the uncertainty of hiatuses in the stalagmite. Aridity, vegetation cover and glacial-interglacial cycles can cause hiatuses and disturb the age model, although the sub-tropical location of the island should minimize the extent of these hiatuses (McDermott et al., 2006; McDermott, 2004).

3.2. Ultraviolet and X-ray photos

The image of the La Vierge stalagmite under visible light shows some alternation between milky-white and more transparent layers. The picture was taken before scouring, so the diagonal scouring grooves are still visible (figure 7.3). When looking at the stalagmite with ultraviolet and X-ray radiation, layering becomes more detailed. Transparent banding becomes more visible with UV radiation, whereas banding in the milky-white areas can better be seen under X-ray. In the milky base, the sample path lies to the right side of the growth axes since layering in the right shoulder was more distinct (figure 7.1 and 7.2).

3.3. XRF-scan

The XRF-scan showed highest values in calcium. The magnesium and aluminum content in the stalagmite are undetectably low. Barium content does not show any correlation with the alternating bands in the stalagmite. The Sr/Ca shows a different correlation between the first calcium dip and the second dip (figure 8). Correlation between calcite content and whiteness of the layers is indicated with orange bands in figure 8. The milky layers tend to have lower calcite content. XRF-scans of important elements can be found in the appendix.

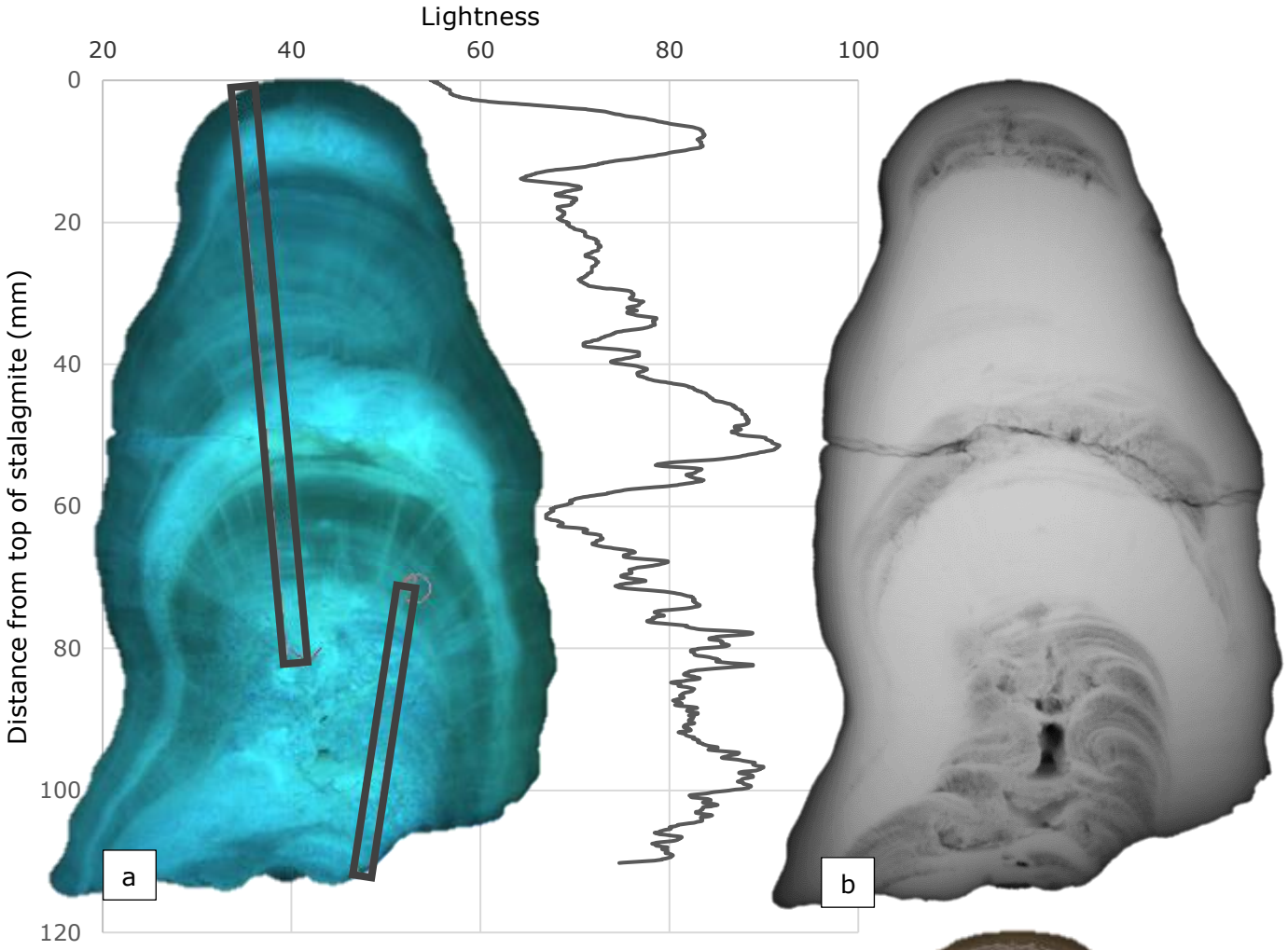

Figure 7. The La Vierge stalagmite as seen under ultraviolet (UV) radiation (top-left figure; a), X-ray radiation (top-right figure; b) and with a digital Color Line Scan Camera (bottom-right figure; c).
The UV image was taken with an exposure time of 20ms through an f/2.8 aperture. Color data was calculated over the rimmed black areas and expressed in lightness, shown in the graph right of the UV image. The right image shows the La Vierge stalagmite under X-ray radiation, exposed to 50kV for 120s. The color image of the La Vierge stalagmite is taken before scouring; the diagonal sawing grooves are still visible. Scans and photos a and b, are made with the Avaatech scanner located at the NIOZ institute, Texel, the Netherlands. For the precise specifications, one can visit http://www.avaatec.

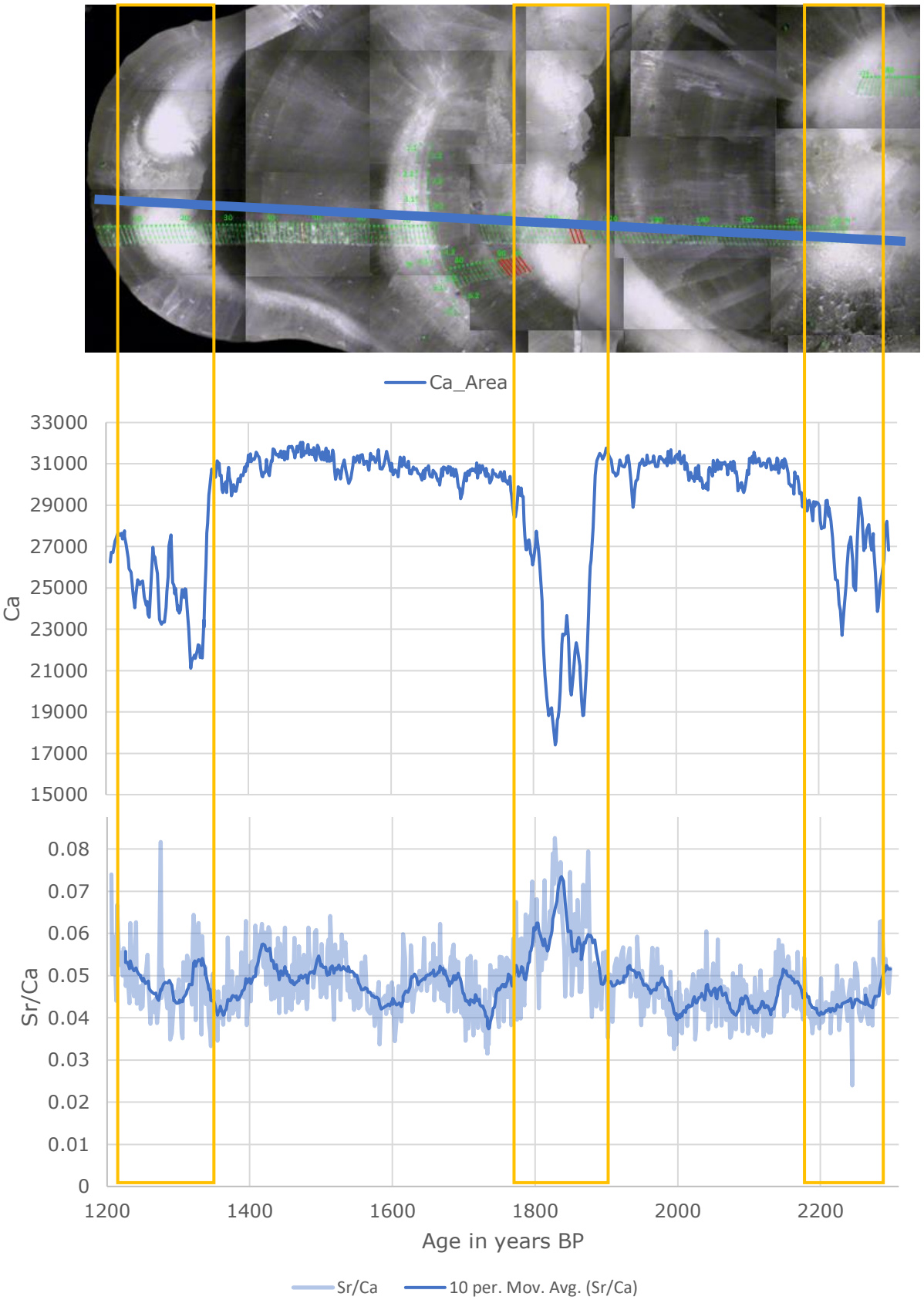

Figure 8. Correlations between calcium density in counts (top graph) and sample location map of the La Vierge stalagmite. Calcium density measured with an Avaatech XRF-scanner over an 82 mm transect (blue line in top figure). The bottom graph shows the strontium/calcium with a darker blue 10-moving average. For more specifications, visit http://www.avaatech.com/. The age model was determined from the two U/Th measurements, see section 2.4.

3.4. Crystallography

Clumping occurs different per type of carbonate. Therefore, the type of carbonate should be determined. Although no high-scale resolution microscopic pictures are available from the stalagmite, the XRF data can tell you the type of carbonate as well (Perrin et al., 2014). In calcite stalagmites, this would be the other way around. Dolomite can form only if the Mg/Ca ratio exceeds 5-10:1 (Folk and Land, 1975). This stalagmite had undetectable magnesium values and relatively abundant strontium values; the stalagmite is assumed to be aragonite.

Additionally, Mg/Ca and Sr/Ca ratios are indicators for the residence time of the meteoric water. Since the Mg content was below detection limits, only the Sr/Ca is plotted in figure 8. The values in the stalagmite will therefore closely reflect environmental changes.

3.5. Hendy test

The results to test whether the stalagmite was deposited under isotopic equilibrium is shown in table 1 and figure 9. Two tests were performed along two different bands. Six samples were taken by drilling 2 mm lines, 0.5 mm deep and 0.5 mm apart along the same growth band. Sample size varied with the density of the stalagmite. Samples in the milky-white layers were drilled at a greater drilling depth as samples in the transparent layers to get the same sample sizes.

When comparing the smaller sized tubes with the bigger ones, little or no difference was seen in average amplitude size. Per sample, the amplitude size did decrease faster over the six measurement cycles when using smaller tubes; since there is a smaller volume and the same input of Helium gas, flushing occurred at a faster rate. Because of the larger difference in amplitude, the fault marge will increase. With this information, it is recommended to use larger sized tubes if possible.

The Hendy test was performed twice on two different layers; one in a transparent and one in a milky-white band (figure 6 and 9). If kinetic fractionation occurs during growth, rapid/uneven loss of CO_2 from the speleothem surface causes precipitated calcite enriched with ^{18}O and ^{13}C. Speleothems cannot be used for research if kinetic loss has occurred during growth (Hendy, 1971).

In table 1, standard deviation (SD) expresses the variability in the results. The highest variation, 0.328 ‰, is found in $\delta^{13}C$ of the first test, mostly caused by sample 6. The Hendy test results (figure 9 and table 1) show that the isotope values do not change significantly when moving along the growth band. There seems to be a trend in the milky-white layer where isotope values enrich away from the apex. Also, the correlation coefficient R^2 reflects there is no relation between $\delta^{13}C$ and $\delta^{18}O$. Thus, during the stalagmite formation no kinetic isotopic fractionation has occurred, meaning that the rate of CO_2 loss was evenly distributed over the speleothem surface and the reliability of the isotope results is high.

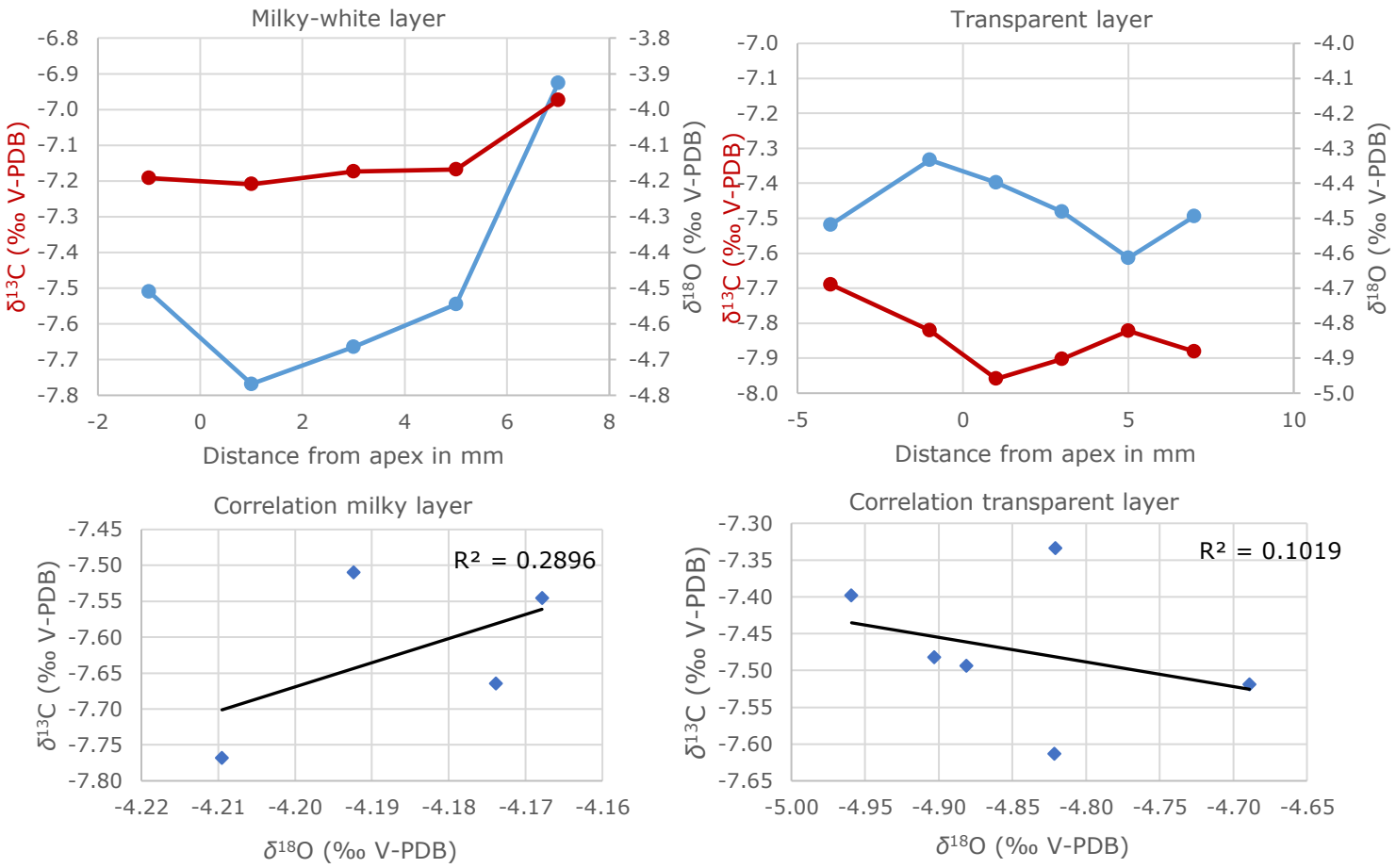

Figure 9. Results of the Hendy tests. Top figures show results from six test samples in the milky-white layer (left) and five test samples in the transparent layer (right). Both carbon as oxygen isotopes were determined and displayed against distance from the apex of the growth band, with on the left y-axes $\delta^{13}C$ values and on the right $\delta^{18}O$ values. Note that all y-axes have a 1‰ scale. Bottom graphs show the correlation between carbon and oxygen isotopes in the two tests. The correlation coefficient R^2 is given in the top-right of the bottom graphs. For the location of the Hendy test samples, see figure 5. All isotope values are given in permilles V-PDB.

Milky layer			*Transparent layer*		
	$\delta^{13}C$	$\delta^{18}O$		$\delta^{13}C$	$\delta^{18}O$
Average	-7.48	-4.14	**Average**	-7.47	-4.85
SD	0.328	0.096	**SD**	0.097	0.093
Min	-7.77	-4.21	**Min**	-7.61	-4.96
Max	-6.93	-3.97	**Max**	-7.33	-4.69

Table 1. Results of the Hendy test over the two layers for oxygen and carbon isotopes. All isotope values are in permilles V-PDB.

3.6. δ^{13}C Analysis

All results of the $\delta^{13}C$ analysis are shown in top graph of figure 10. Values with an amplitude beneath 800 were indicated with red triangles. These values therefore have a lower reliability. Samples with amplitudes lower than 400 were not included in the trend (same accounts for the $\delta^{18}O$ record).

The produced carbon isotope record shows a decreasing linear trend with age (dotted black line in figure 10), from -6.5 to -8.6‰. The formula is shown in the graph with a correlation coefficient, R^2, of ~0.34. Most isotopic variations lie within 1.5 ‰, indicated with a light grey band. Correlation between the location of milky-white bands and drops in the carbon isotope record is shown with orange bands. The dashed line marks the second white band at 35 mm which is not visible in the $\delta^{13}C$ trend. A possible explanation for the non-correlation is that the layer was not broached because of shallow drilling depth of the MicroMill or that this layer is less pronounced (in terms of variability) than the other milky-white layers. The XRF-scan also did not show an increase in calcium in the less pronounced white layer (see figure 8). There is one clearly visible dip in $\delta^{13}C$ in between 1375-1275 BP. The second dip is around 1875-1975 BP, though less distinctive than the youngest one.

3.7. δ^{18}O Analysis

All results of the $\delta^{18}O$ analysis are shown in bottom graph of figure 10. Similar to the $\delta^{13}C$ record, the $\delta^{18}O$ shows a decreasing trend with age, from -4.7 to -5.2‰. Variability in the oxygen isotopes record is much higher than the carbon isotopes record, which is also reflected by the correlation coefficient, R^2, which equals 0.043. Scatter increases when the samples are older than 2400 BP. Where the carbon isotopes in the orange boxes in figure 10 which showed correlation (dip $\delta^{13}C$ in milky-white layers), the oxygen isotopes seem to have little or no correlation of this kind.

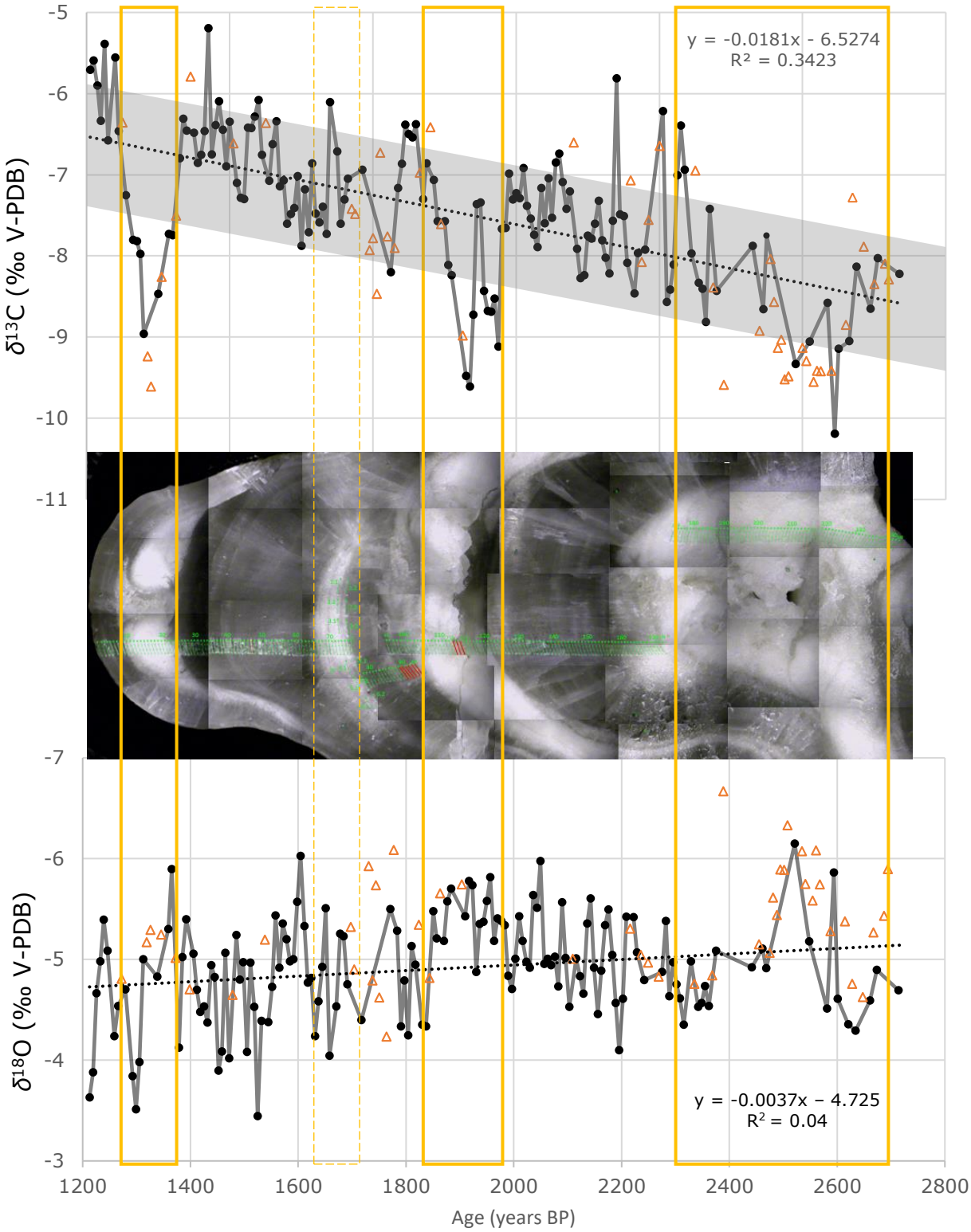

Figure 10. Correlations between the La Vierge stalagmite carbon (top graph) and oxygen (lower graph) isotope record and sample location. All sample locations are indicated in the middle figure; red lines are unsampled. Stalagmite isotope records are plotted against the distance as seen from the top of the stalagmite, with the top being zero. Triangles represent samples with a 400> amplitude <800. Both linear trend lines, the black dotted lines, are expressed in the equations shown in the top right of the corresponding graph. Correlations between trends in the carbon isotope record and the alternating (visual) white bands are indicated with orange boxes. The dotted orange box has a lack of correlation with the isotope trend. The same bands are drawn over the oxygen isotope record. The grey band marks all samples within a ±0.75‰ deviation from the trend line. The age model was determined from the U/Th measurements.

3.8. Correlation δ¹³C and δ¹⁸O

The correlation between carbon and oxygen isotopes is displayed in figure 11. Its correlation coefficient, R^2 is 0.18; although both records show a decrease in isotope value with age, covariance between the two variables is low.

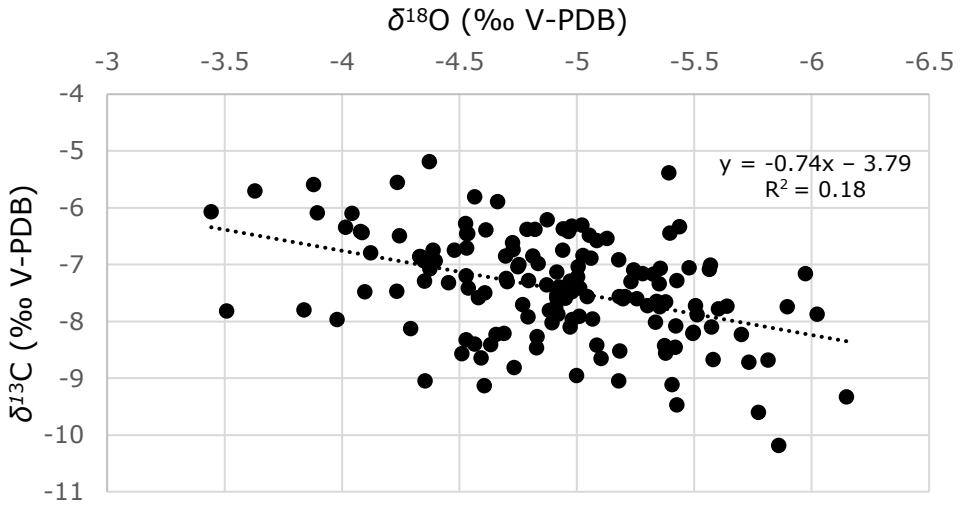

Figure 11. Correlation between carbon ($\delta^{13}C$) and oxygen ($\delta^{18}O$) isotopes. The equation of the dotted linear trend line is shown in the top right of the graph as well as the correlation coefficient, R^2.

3.9. REDFIT Analysis

REDFIT spectral analysis was done at two confidence intervals, namely 95% and 99%; Significant frequencies have a power above the confidence interval. REDFIT frequency analysis was executed on the element Sr, on the Sr/Ca ratio and the isotope records. REDFIT frequency analysis on strontium shows a cyclicity in the element over 291, 134 and 9 years (figure 12). The Sr/Ca shows a cyclicity of 9.5, 109, 155 and 364 years (figure 13). Figure 14 shows a cyclicity within the oxygen isotope record of about 24, 33 and 40 years. The carbon isotope record captures a similar cyclicity of about 28, 43 and 48 years (figure 15).

Thus, while the cyclicity found in the isotope values show a decadal cyclicity, the cyclicity in calcium and strontium is more centennial or yearly.

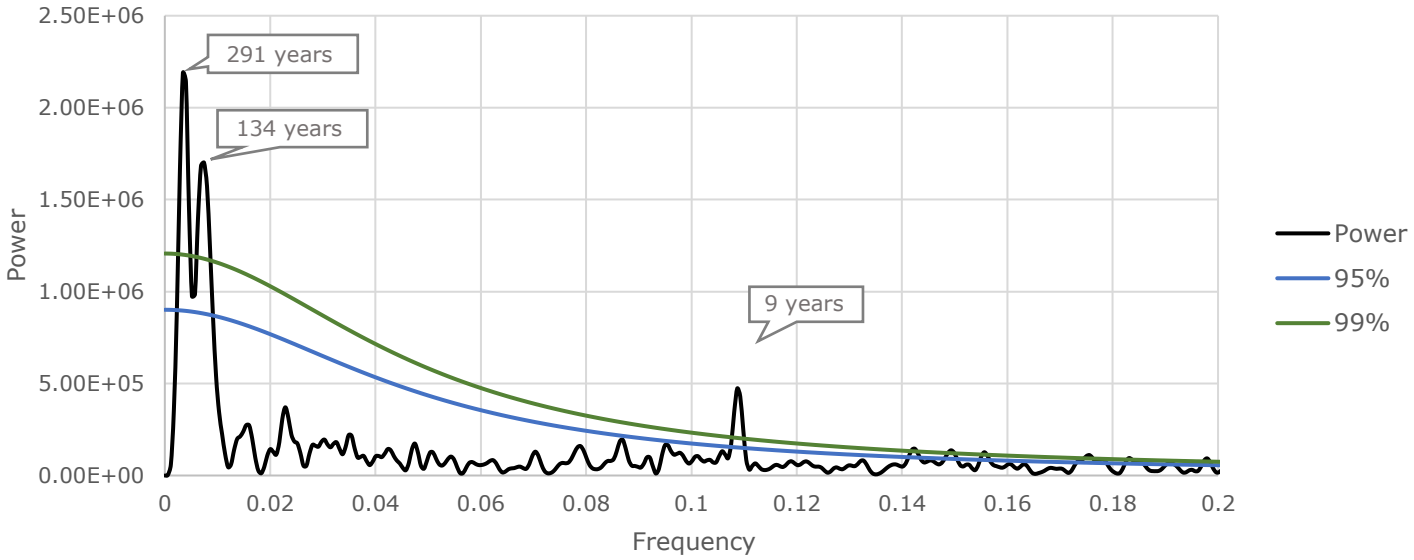

Figure 12. REDFIT frequency analysis of strontium content in the stalagmite. Confidence intervals (95-99%) indicate a cyclicity of 291, 134 and 9 years. Significant cyclicity is labeled on the graph in years. Figure made with PAST.

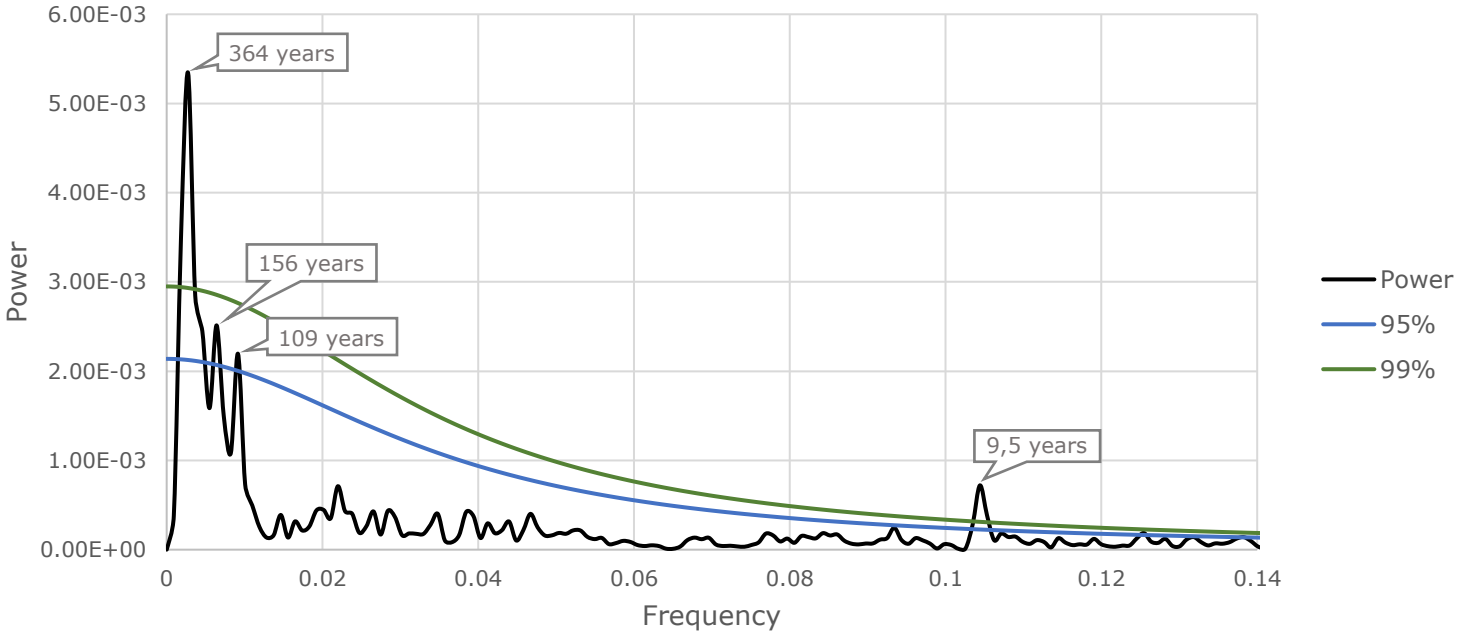

Figure 13. REDFIT frequency analysis of Sr/Ca content in the stalagmite. Confidence intervals (95-99%) indicate a cyclicity of 364 and 9.5 years. The smaller peaks correspond to a 155 and 109 year cyclicity. Significant cyclicity is labeled on the graph in years. Figure made with PAST.

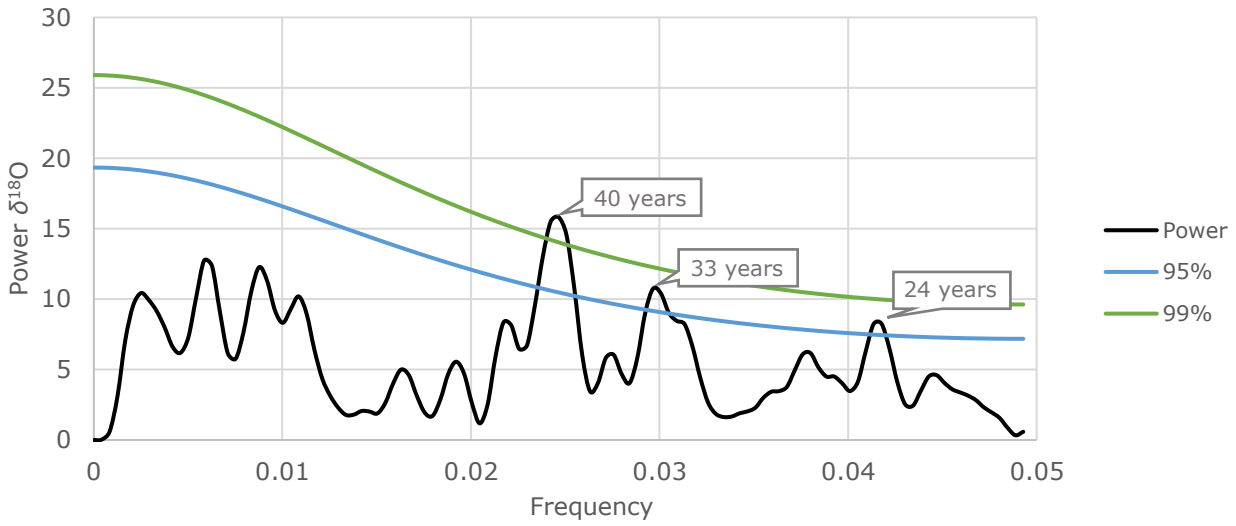

Figure 14. REDFIT spectral analysis of the oxygen isotope record. Significant confidence intervals (95-99%) are indicated with significant cyclicity in years.

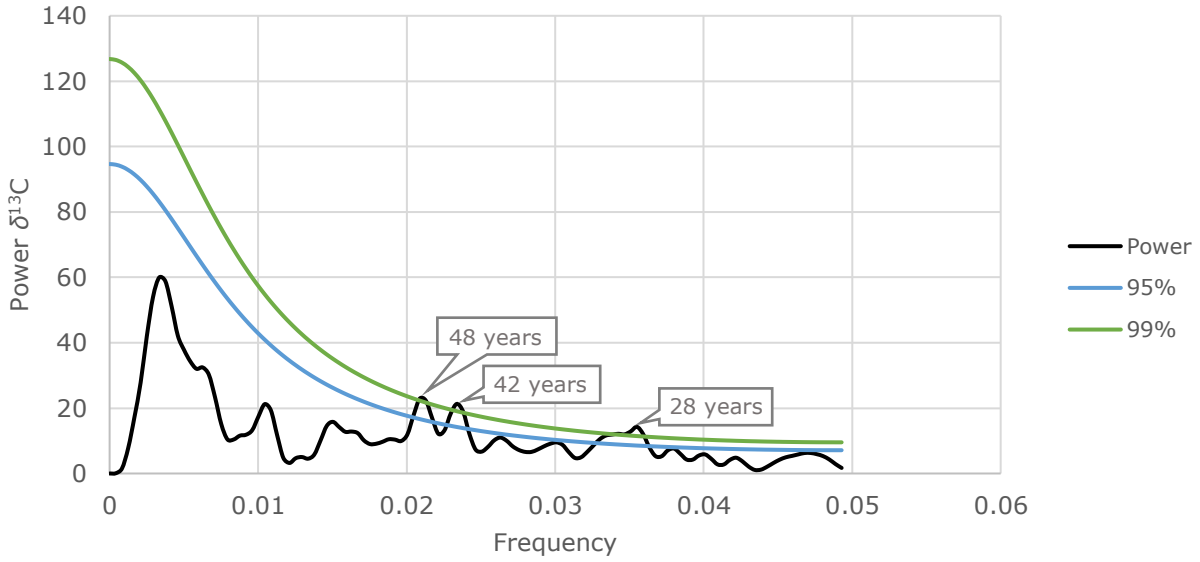

Figure 15. REDFIT spectral analysis of the carbon isotope record. Significant confidence intervals (95-99%) are indicated with significant cyclicity in years.

3.10. Wavelet analyses

The wavelet analyses of both the carbon (figure 16) and oxygen (figure 17) isotopes show a cyclicity over the record of about 300 years. It can be noted that the carbon isotope record includes higher significance in cyclicity than oxygen isotopes; the carbon isotopes also include smaller scale cyclicity compared to the oxygen isotopes. However, the yearly cyclicity found in the strontium content is not found in either of the isotopes.

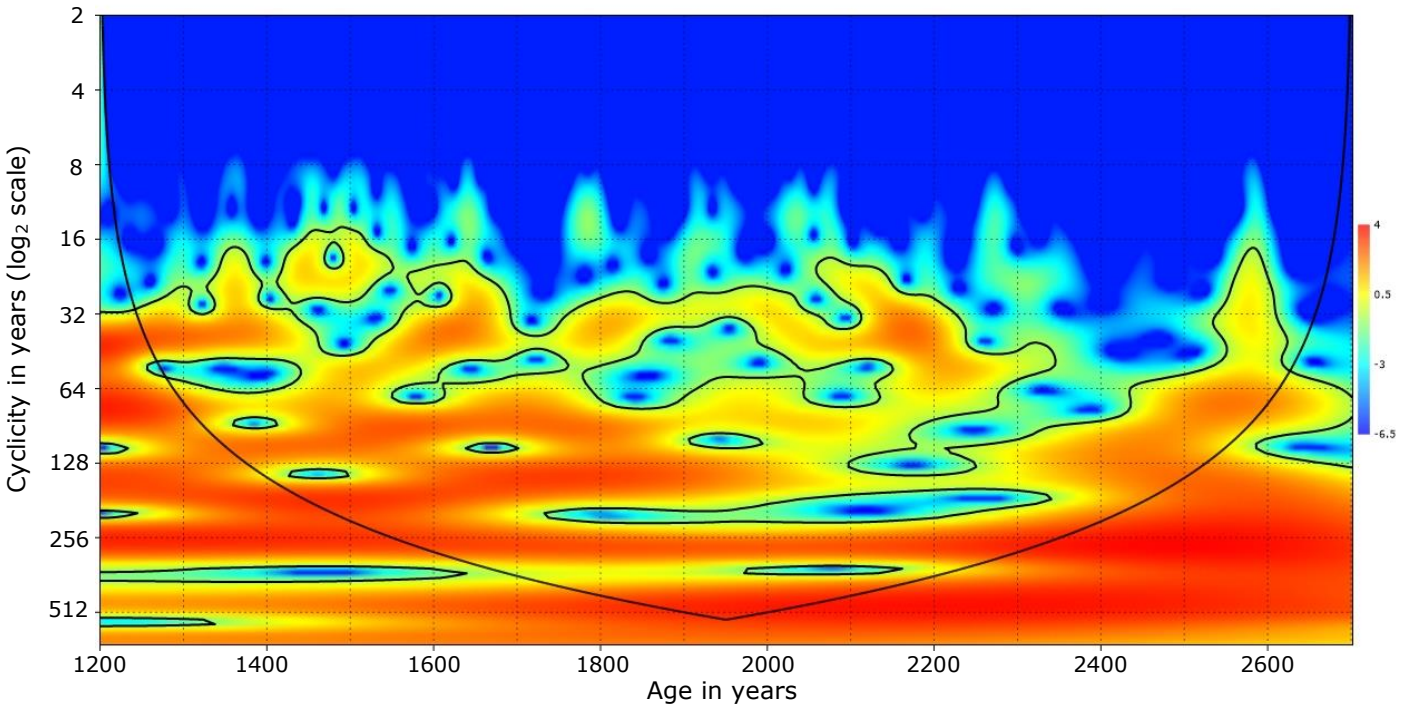

Figure 16. Wavelet analysis on $\delta^{13}C$ over the 1550-year record displayed as a contour plot. The contour bar is shown on the right. Red fields are periods of high cyclicity of the corresponding y-value. Note that a $\log^2$ scale is used on the y-axes. Black lines around the contours indicate a significance level of p=0.05. The cone of influence is indicated as a black line. All values are given in years.

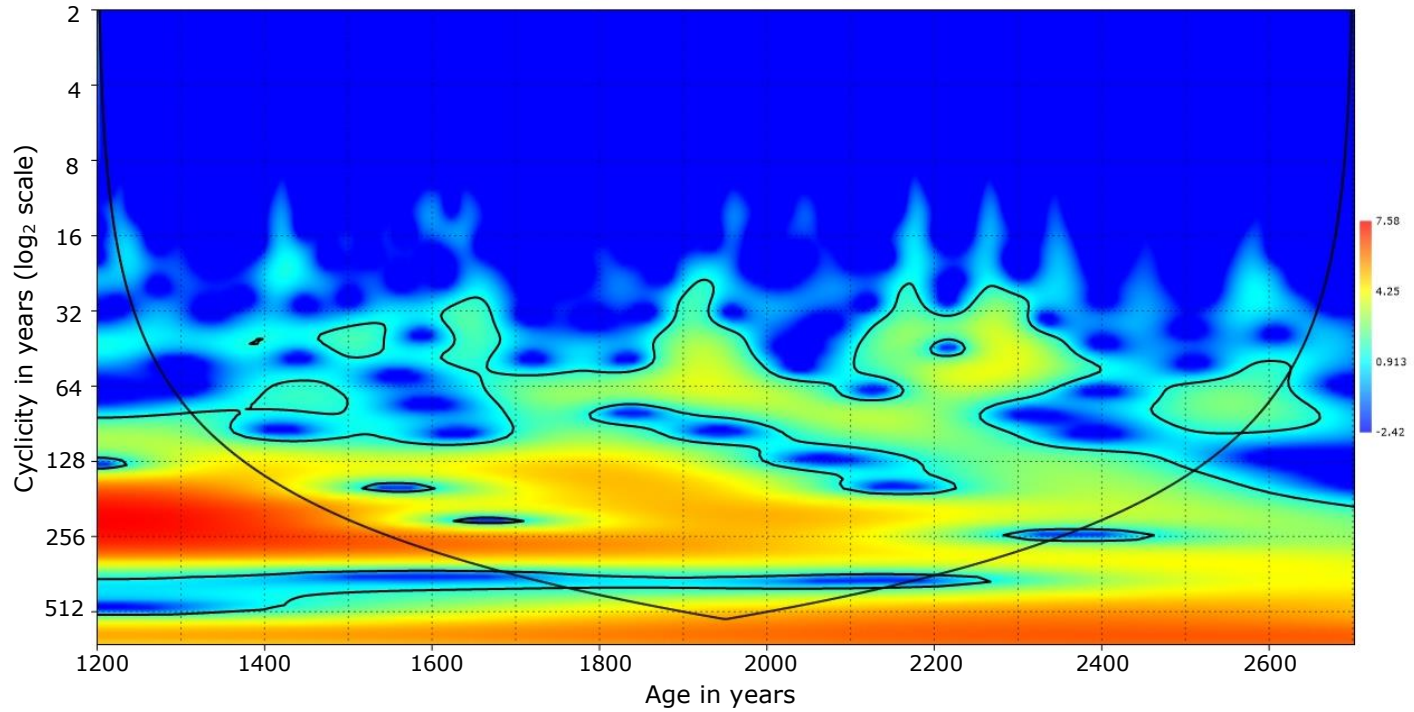

Figure 17. Wavelet analysis on $\delta^{18}O$ over the 1550-year record displayed as a contour plot. The contour bar is shown on the right. Red fields are periods of high cyclicity of the corresponding y-value. Black lines around the contours indicate a significance level of p=0.05. The cone of influence is indicated as a black line. Note that a $\log^2$ scale is used on the y-axes. All values are given in years.

3.11. Gaussian bandpass filter

Gaussian bandpass filters were applied on the strontium, carbon and oxygen record. Amplitude size reflects the presence of significant cyclicity in the record. Three significant cyclicities in the strontium record were applied as bandpass filter. The significant cyclicities are 9, 134 and 291 years. Figure 18 shows the 9-year cyclicity with a bandwidth of 0.01 ‰ with a positive correlation over the strontium record. Variations in power can be observed over the record. The variability in amplitude size is caused by a combined effect of the other significant cyclicities. Three significant cyclicities in the carbon record were applied as bandpass filter on the data: 28, 43 and 48 years. Figure 19 shows the 40-year cyclicity with a bandwidth of 0.002 ‰ with a positive correlation over the carbon record. Three significant cyclicities in the oxygen record were applied as bandpass filter on the data: 24, 33 and 40 years. Figure 20 shows the 42-year cyclicity with a bandwidth of 0.001 ‰ with a positive correlation over the oxygen record. The dominance in the 42-year cyclicity is increasing over time.

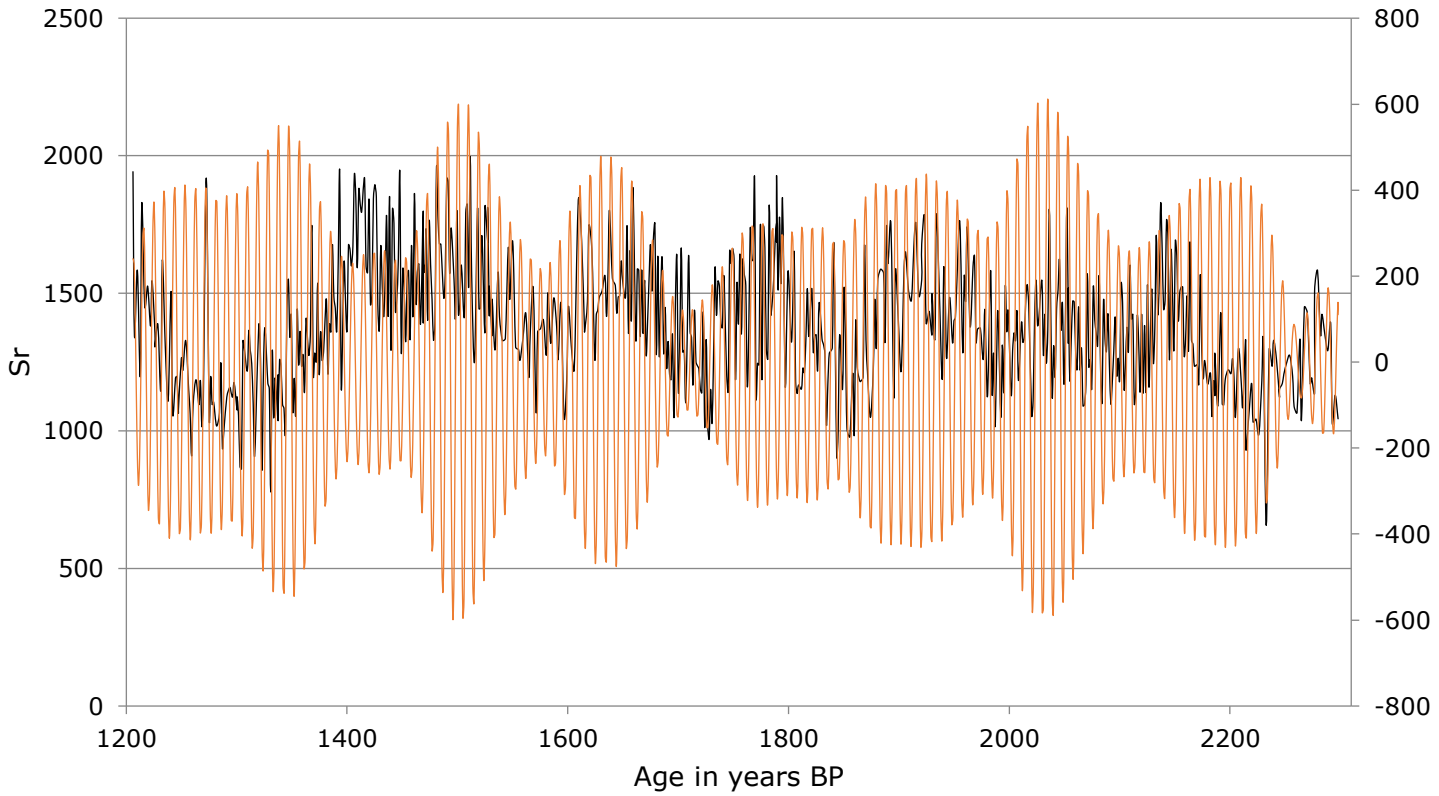

Figure 18. Gaussian bandpass 9-year filter (orange) applied on the strontium density (black) over time. A bandwidth of 0.01‰ was applied. Strontium density is measured with an Avaatech XRF-scanner over an 82 mm transect (figure 8) and indicated in counts. For specifications about the Avaatech scanner, visit http://www.avaatech.com/. The age model was determined from two U/Th measurements, see section 2.4.

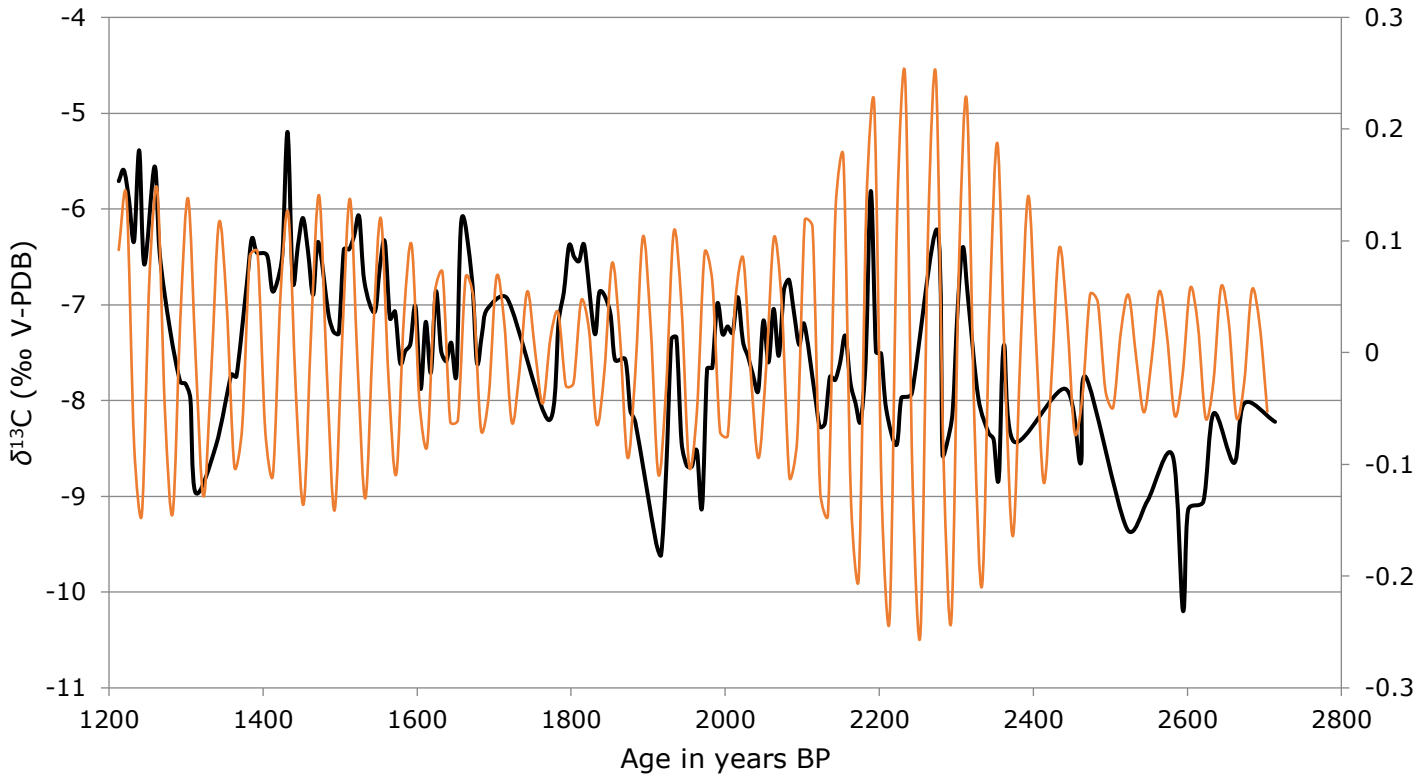

Figure 19. Gaussian bandpass 40-year filter (orange) applied on the carbon isotope record (black) over time. A bandwidth of 0.002‰ was applied. The age model was determined from two U/Th measurements, see section 2.4.

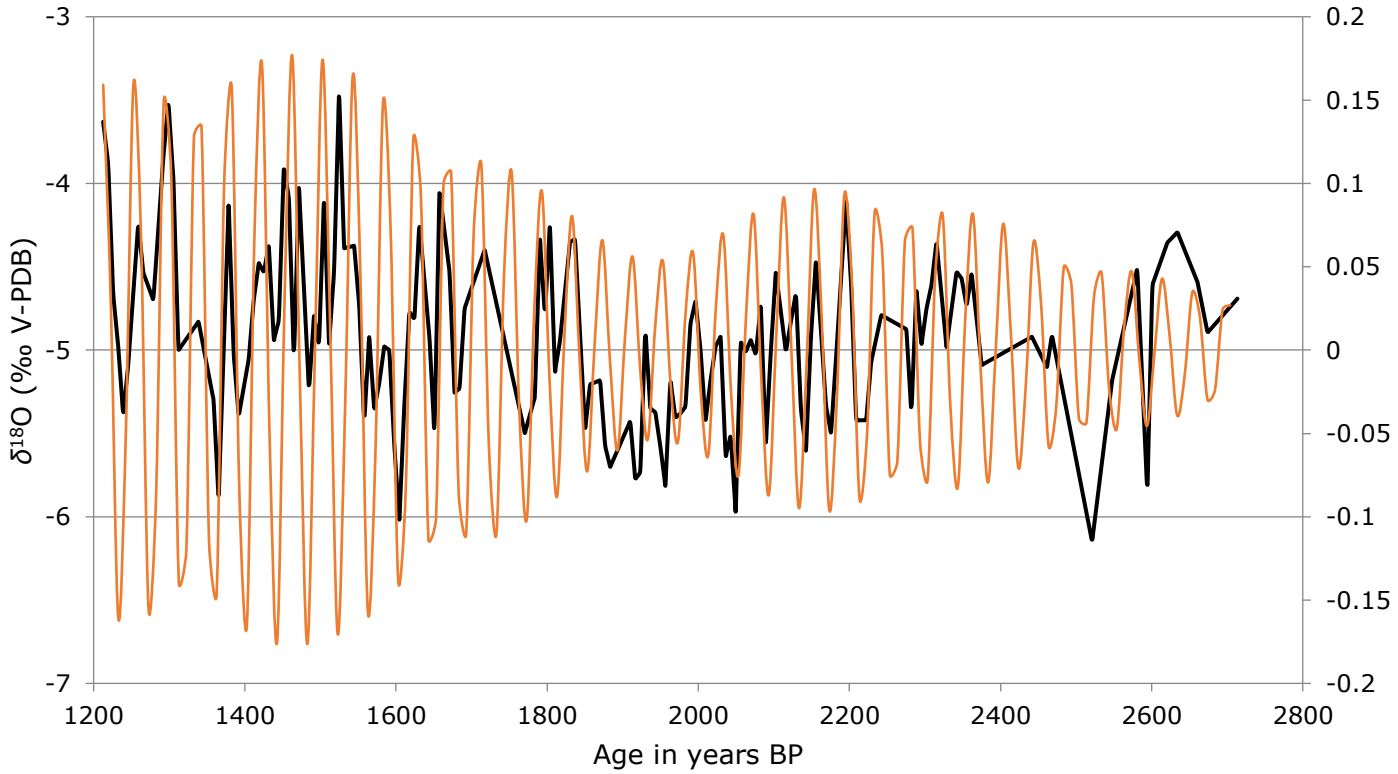

Figure 20. Gaussian bandpass 42-year filter (orange) applied on the oxygen isotope record (black) over time. A bandwidth of 0.001‰ was applied. The age model was determined from two U/Th measurements, see section 2.4.

3.12. Clumped isotopes

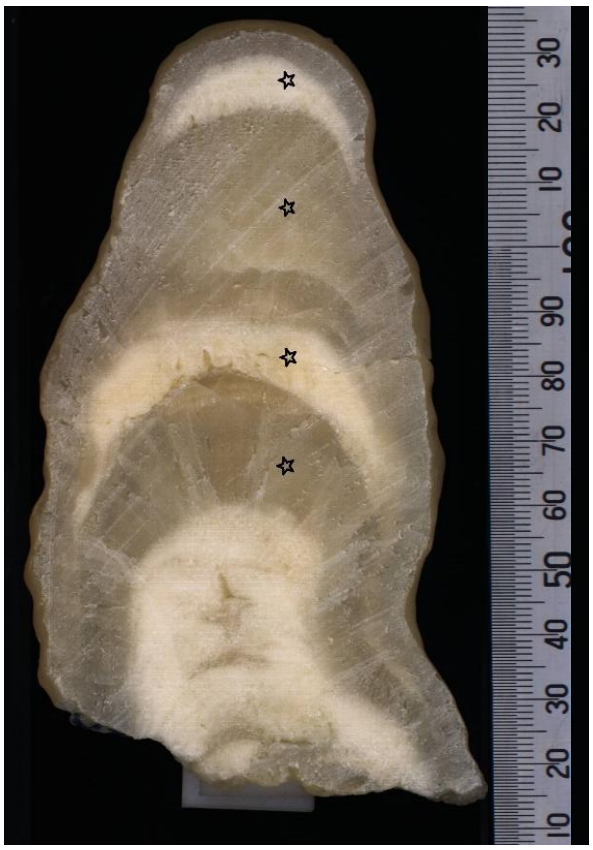

Figure 21. The four sample locations for measuring the clumped isotopes value (Δ_{47}) indicated as black stars. The locations are based on variations in the isotope record (figure 10). Color made on NIOZ, Texel with a digital Color Line Scan Camera

The four locations for the clumped isotope measurements are indicated in figure 21. The four locations are two sets of two which show strong $\delta^{13}C$ shift between them.

Table 2 gives the number of aliquots per sample, the correlation coefficient (c), the W-value and the p-value. In sample RS-4, there was one abnormality. The RS-4c, gives the correction without this sample to show the difference. The first sample gives the highest values whereas the uncorrected sample RS-4 gives the lowest. The RS-4 samples not follow normal distribution and therefore the standard deviation cannot be determined. This RS-4 sample is first to be rejected from the null-hypothesis, but when sample 10, with a Δ_{47} of 1.712 is removed from the hypothesis, the samples follow a normal distribution. This sample is then therefore not used to calculate temperature. The clumped data was analyzed statistically using QQ-plots and boxplots. An overview of the samples was given in a boxplot in figure 22. All clumped isotopes QQ-plots can be found in figure 23. The summary of all QQ-plots is given in figure 24.

Temperatures calculated with the Kele [2015] give all relatively high temperatures, whereas the Meckler [2014] calibration gives more representable values (table 4). In both calibrations, a decrease in temperatures is visible towards the top. Median values show smaller scatter than average values (table 3), which is an indicator of the amount of scatter within the samples. Increase in bias is found with increase in Δ_{47} value. Temperatures are compared with values derived from equation 1. The $\delta^{18}O_{water}$ used was -2.25 ‰ (Spliethoff, 2015). When filling in, the average temperature was 28.2 °C. The general trend was cooling over the 1550 years, see figure 25. However, the standard deviation is larger than the decrease in temperature.

Name	Aliquots	c	W	p	Δ_{47}	Δ_{47} SD	Δ_{47} Q2	ΔQ2-average
RS-1	5	0.99	0.98	0.95	0.663	0.053	0.665	0.002
RS-2	13	0.96	0.91	0.21	0.649	0.069	0.673	0.024
RS-3	14	0.97	0.93	0.30	0.660	0.086	0.658	0.002
RS-4	12	0.79	0.64	0.0003	0.746	-	0.643	0.103
RS-4c	11	0.98	0.97	0.89	0.657	0.112	0.639	0.018

Table 2. Summary of the clumped isotopes results including sample name, number of aliquots, the correlation coefficient, the W-value, the p-value, average Δ_{47}, its standard deviation and the median (Q2) of the Δ_{47} samples. The temperature was calculated both from the average and median Δ_{47} value. Lastly, the differences in average and median was listed. All isotope values are in permilles.

Type of calibration	*Kele [2015]*		*Meckler [2014]*	
Used data	**Δ_{47} average**	**Δ_{47} Q2**	**Δ_{47} average**	**Δ_{47} Q2**
RS-1	36.8	36.3	28.4	27.7
RS-2	41.7	33.6	32.8	25.3
RS-3	29.1	38.8	29.3	30.1
RS-4	12.0	44.1	5.4	35.0
RS-4c	38.9	45.4	30.3	36.1

Table 3. Temperatures calculated according to two different calibrations. The Kele [2015] calibration based on travertines, the Meckler [2014] calibration based on synthetic calcite precipitation. Temperatures are calculated with the average Δ_{47} values and median values to correct for non-normally distributed data. All isotope values are in permilles.

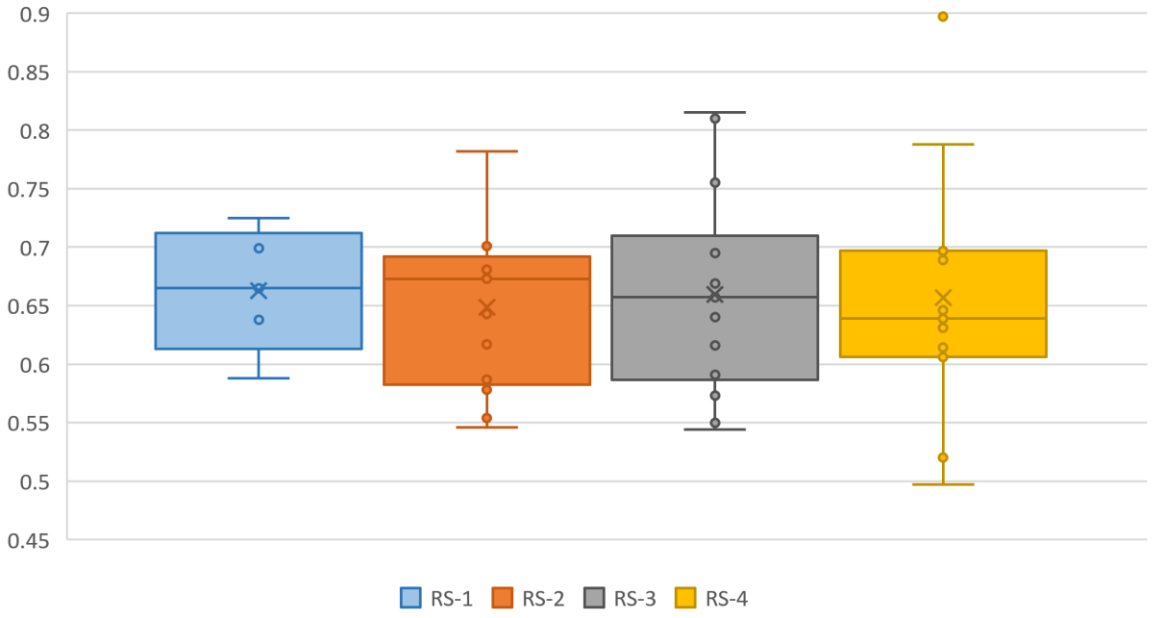

Figure 22. Boxplot of all clumped isotopes. The box shows the 1st and 3rd quartile and median (Q2) value in the middle. Whiskers indicate maximum and minimum values. One outlier is found in RS-4.

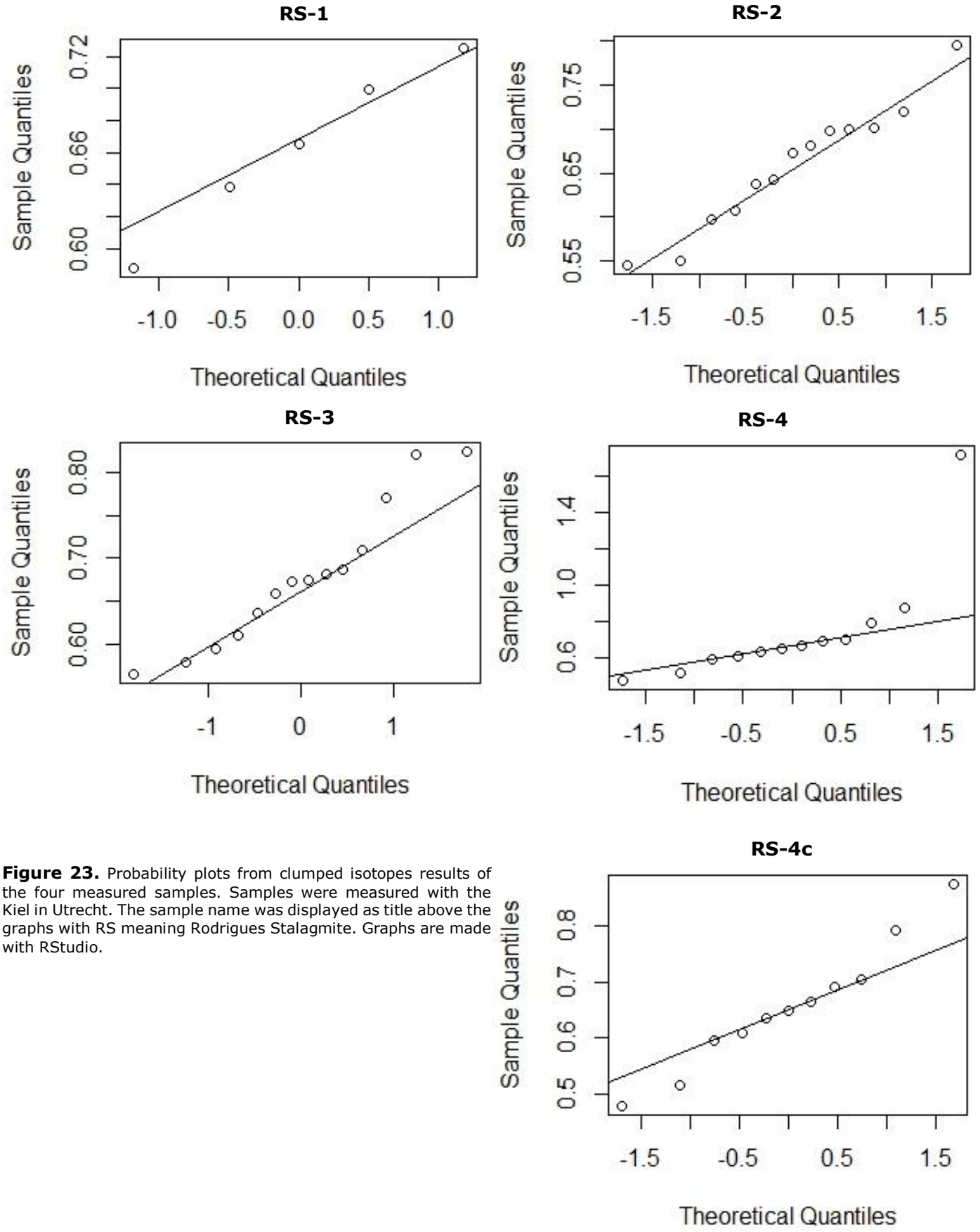

Figure 23. Probability plots from clumped isotopes results of the four measured samples. Samples were measured with the Kiel in Utrecht. The sample name was displayed as title above the graphs with RS meaning Rodrigues Stalagmite. Graphs are made with RStudio.

Aliquots	43
c	0.99
W	0.98
p	0.61
Δ_{47} average	0.656
SD Δ_{47}	0.083
Kele T(°C)	39.2
Meckler T(°C)	30.6

Table 4. Summary of all clumped isotope statistics.
With c (correlation coefficient), the W-value, the p-value, Δ_{47} with its standard deviation and thereafter calculated average temperature calculated with two different calibrations; the travertine calibration by Kele et al. [2015] and the synthetic calcite calibration by Meckler et al. [2014].

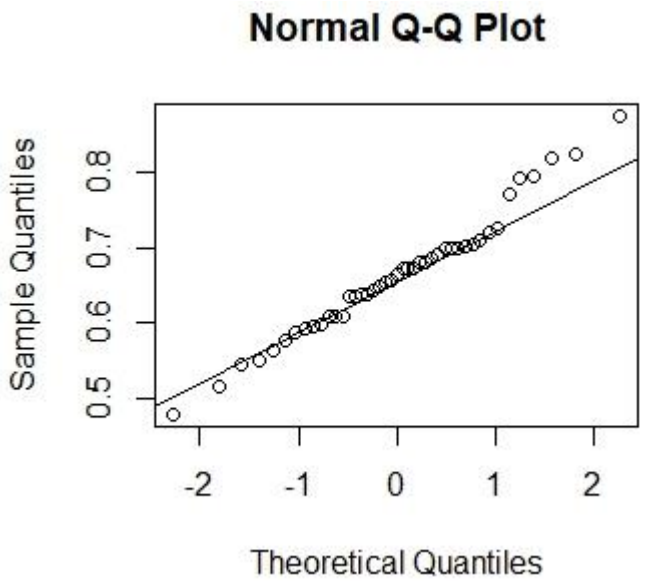

Figure 24. Probability plot of all clumped isotope results, assuming temperature difference was insignificant.

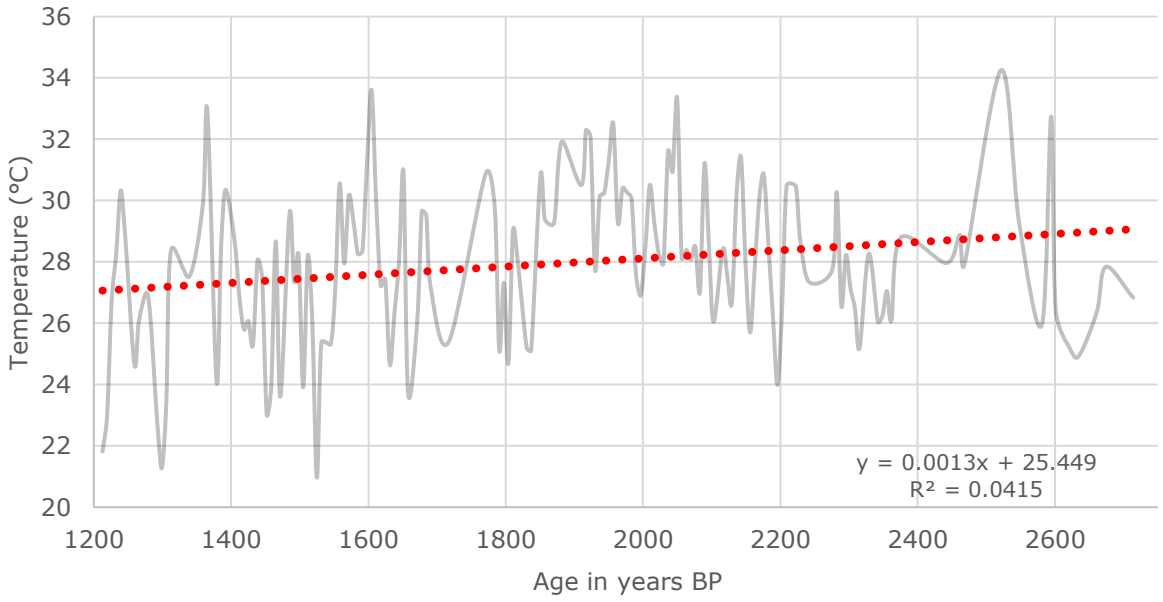

Figure 25. Temperatures calculated from the oxygen isotope record using in situ fluid inclusions from the MSc Thesis from Spliethoff [2015]. Showing a cooling linear trend over the stalagmite with a relatively large scatter. The formula and correlation coefficient (R^2) are displayed on the graph.

Discussion

4.1. Formation of stalagmites

Formation of stalagmites can occur in two kinds of caves:

- Primary caves, which form during the formation of the rock. Examples are lava tubes and cave blisters (van Breukelen, 2009).
- Secondary caves are formed by dissolving acidic water. The most common speleothems are formed in secondary caves in calcareous rock bodies, mainly limestone. These speleothems consist mainly of calcium carbonate ($CaCO_3$). As water percolates through the soil, it is acidified by respired CO_2 or by available CO_2 in the soils on top of the limestone rock (van Breukelen, 2009; Hendy, 1971). Dissolution of calcareous rock occurs through equation 7 and 8. The solubility of the $CaCO_3$ depends on the partial pressure in solution (Garrels and Christ, 1965)

$$CO_2 + H_2O \rightarrow H_2CO_3 \qquad \text{eq. 7}$$

$$H_2CO_3 + CaCO_3 + H_3O^+ \rightarrow Ca^{2+} + HCO_3^- \qquad \text{eq. 8}$$

When the percolated water enters the cave, it drips from the ceiling. The humidity in caves lies around 95-100% which minimizes the amount of evaporation and promotes precipitation of the $CaCO_3$ minerals to form new layers on speleothems (McDermott et al., 2006).
Since the water has an increased concentration of CO_2, degassing occurs. With the degassing of CO_2, $CaCO_3$ is deposited, shown in equation 9.

$$Ca^{2+} + 2\ HCO_3^- \rightarrow CaCO_3 + CO_2 + H_2O \qquad \text{eq. 9}$$

Within the cave, crystal growth disturbance is minimal. Therefore, drip water chemistry is mostly externally influenced (van Breukelen, 2009; Dorale and Liu, 2009; Hendy, 1971; McDermott et al., 2006). Over time, new thin film layers, about 100 µm thick, of deposited carbonate cause growth of these speleothems. The visible layering in stalagmites is caused by inclusion of organic matter or changes in growth rate (Genty et al., 2001).

During the formation of new layers on speleothems, altering of the crystal structure can create cavities. These cavities can either be caused by intrusion of organic material or by CO_2 gas. Later, these cavities can be filled with cave drip water, which can become trapped during the ongoing formation of the speleothem (Kluge et al., 2008). This trapped cave drip water in the cavities are called fluid inclusions. Because of the fluid inclusions, these layers have a lower density than layers with no fluid inclusions (van Breukelen, 2009). Closed off from external influences, these fluid inclusions can be a proxy for paleo-rainfall and act as an indicator for increased growth if homogenization in the fluid inclusion water is assumed and corresponding age of the paleo-water with the surrounding carbonate. (Kendall and

Broughton, 1978). The ultraviolet and X-ray photos showed that the milky-white layers have lower density (figure 7 and 8), which can be linked to periods of higher rainfall. Also, when comparing the transparent layer to the milky-white layer in the Hendy test, the $\delta^{13}C$ deviated from the apex in the milky-white layers, whereas the difference in the transparent layers was minimal. Thus, in milky-white layers, some kinetic fractionation occurred when moving away from the apex (within 1‰). This can be linked to increased drip rate. This could indicate higher rates of percolation during an increase in either temperature and/or humidity (Genty et al., 2001). Since these climate variabilities would not only have local effect, it is expected that the trends found in this speleothem can be correlated to other speleothems in the region (van Breukelen, 2009; Feng et al., 2014).

Fractionation away from the apex does not imply that fractionation occurred in the apex itself, since theoretically isotopic equilibrium could be reached at the same time in the apex when not at the flanks (Dorale and Liu, 2009; Kotlia et al., 2012). So, even with failing the Hendy test in the milky-white layers, the stalagmite can still be used to reconstruct paleo-rainfall (Kotlia et al., 2012). Clumped isotope measurements can help detect equilibrium fractionation as well (Kluge and Affek, 2012). Kluge and Affek [2012] also add that with increasing growth rate, a supersaturation is not reached always, which will hamper new layers to reach an isotopic equilibrium.

4.2. $\delta^{18}O$ variations

The $\delta^{18}O$ is affected by the several factors, three of them will be discussed hereafter. A schematical overview is given in figure 26. The first is the salinity effect: when the ratio evaporation/precipitation increases, $\delta^{18}O_{water}$ increases. Secondly, the ice volume effect: when the ratio (global) ice melt/ice growth increases, $\delta^{18}O_{water}$ decreases (Grant et al., 2012) and lastly the temperature effect; when temperature increases, $\delta^{18}O_{water}$ decreases (Ravelo and Hillaire-Marcel, 2007). The combined effect will influence the local hydrology and with that the isotopic value in the stalagmite. For example, a Mediterranean stalagmite (semi-arid area) included varying $\delta^{18}O$ values from -6‰ to -3.7‰ over one seasonal cycle because of local hydrologic variability (Bar-Matthews et al., 1996). Rodrigues has a subtropical, maritime climate with relatively stable yearly temperatures; the so called "amount effect" is most significant in this climate region (Feng et al., 2014; Lachniet, 2009; Ravelo and Hillaire-Marcel, 2007). The amount effect refers to the net effect of kinetic fractionation due to precipitation and evaporation. When there is an increase in environmental precipitation, heavier isotopes (^{18}O) are more likely to precipitate, leading to a different isotopic composition of precipitation (Bar-Matthews et al., 1996; Dansgaard, 1964). Since precipitation variability changes the isotopic composition of meteoric water, monthly to annual intervals with higher precipitation, like monsoons, as well as small episodes with higher precipitation, like cyclones, will be characterized by a depletion of heavier isotopes in the atmosphere. This will lead to

lower $\delta^{18}O$ values that can condensate and eventually lower $\delta^{18}O$ in the precipitated carbonate forming the speleothem (Huntington et al., 2009; Lee et al., 2008). The throughflow of the meteoric water through the karstic overlying bedrock will determine how much of the varying signal is found in the isotopic value; when throughflow is very slow, the $\delta^{18}O$ will be an average signal over a longer time. This in turn enables the speleothem to reflect either on inter- or intra-annual variability (Bar-Matthews et al., 1996; McDermott et al., 2006). This signal can also be picked up by element ratios in speleothems, which is described earlier. Thus, there are many signals causing fluctuations in $\delta^{18}O$. It depends on drip rate, percolation time and region which signal is dominant (Bar-Matthews et al., 1996; McDermott et al., 2006).

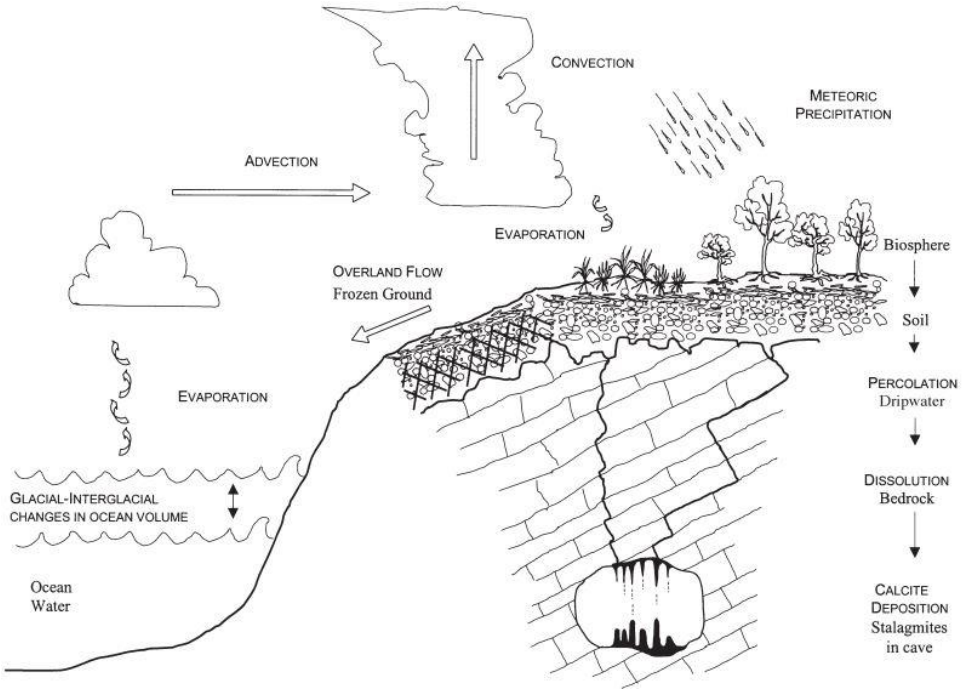

Figure 26. Schematic overview of the factors influencing isotopic variability externally and during percolation before stalagmite formation (apart from direct global temperature). The oxygen isotope signal reflects cave temperature and the isotopic composition of meteoric water. Carbon isotopes include bedrock, soil, atmospheric and gas sources. Before evaporation, seawater chemistry can vary by changing sea level, mainly by locking away fresh water in ice. From the moment of evaporation to precipitation over the soil, distance and altitude will change the isotopic value of the water vapor will change due to kinetic fractionation. Carbon isotope values are then also altered by the biosphere since isotopic value of the soil changes with age and thickness of the soil. As the water percolates through the carbonate rock, isotopic variability occurs due to dissolution of the surrounding $CaCO_3$ bedrock and acidification due to respired CO_2. Lastly, variability in percolation time and drip rate can result in variability of the isotopic composition in speleothems. Figure by Lauritzen and Lundberg, 1999.

Additional factors influencing the $\delta^{18}O$ include the effect of raindrop size; the larger the raindrop the longer it takes before isotopic equilibrium takes place. And when relative humidity decreases, there is an increase in heavy isotope content (Lee et al., 2008). Other effects contributing to the amount effect is the location of the cave (as mentioned above) and its altitude and distance relative to the sea (McDermott et al., 2006). Thus, it should be considered that the $\delta^{18}O$ values reflect fractionation by precipitation and temperature at moment of deposition as well as location-based effects. Additionally, the calcite-aragonite

mineralogy influences the equilibrium fractionation factors (Frisia et al., 2002; Grossman and Kiu, 1986; McDermott et al., 2006; Lachniet, 2009). The temperature offset by using a different fractionation effect or a different paleotemperature formula is critical and can lead to a bias of several degrees (McDermott et al., 2006).

There are three possible ways of using fluid inclusions to measure temperature. First, through liquid-vapor homogenization of fluid inclusion water, second by the content and ratios of noble gas concentrations dissolved in fluid inclusion water and third by the partitioning of oxygen isotopes between fluid inclusion water and calcite (van Breukelen, 2009; Krüger et al., 2011; Kluge et al., 2008; Meckler et al., 2015). The fluid inclusions used to calculate temperature from the thesis by Spliethoff [2015] used the third technique. The value of $\delta^{18}O_{water}$ positively correlates with temperature. The scatter found in figure 20 can therefore be reduced when specific $\delta^{18}O_{water}$ values from the stalagmite are known over the whole record. However, with applied correction, the general decreasing trend in temperature will remain the same.

4.3. $\delta^{13}C$ variations

There are several mechanisms that can cause the $\delta^{13}C$ fluctuations seen in figure 10. All causes are listed in the order of the formation process of stalagmites and illustrated schematically in figure 26**.** Dissolved CO_2 seeping through the carbonate karst system has two sources: atmospheric CO_2 and respired CO_2. Thus, as $\delta^{13}C$ has a dampened signal, having its source at the bedrock, the $\delta^{18}O$ trend can be caused by changing dominant factors.

4.3.1. Areal

Globally, $\delta^{13}C$ in atmospheric pCO_2 has no fluctuations that can explain the change in $\delta^{13}C$; the value is relatively constant, about ~ -6‰ pre-industrially (Böhm et al., 2002); significant $\delta^{13}C$ decrease (about 1‰) in atmospheric CO_2 occurred with the start of the industrial revolution starting ~1800 AD (Böhm et al., 2002; Pachauri and Reisinger, 2007), a signal too young to be seen in the stalagmite. Thus, the isotopic signal will be reflecting source carbonate influences and respired CO_2. Sea surface productivity fluctuations can alter the dissolved inorganic/organic carbon ratio in the surface ocean; IOD forcing of sea surface productivity increases the $\delta^{12}C$ due to increased respiration. However, chlorophyll increase occurs mostly in the northern Indian Ocean during such an event (Currie et al., 2013). Thus, changes in sea surface productivity is unlikely to be the dominant factor of the $\delta^{13}C$ variability.

4.3.2. Surficial

On the surface above the cave, vegetation and/or soil alterations can cause variation in $\delta^{13}C$ of the seeped CO_2. Vegetation can be classified by their pathway for photosynthesis; C3, C4 or a combination of the two: CAM plants. The $\delta^{13}C$ values are not significantly altered when it is decomposed to soil, so changes in vegetation can correlate to $\delta^{13}C$ variability in the soil

as well (Boutton et al., 1998). The type of vegetation matches its climate; C4 plants include mainly tropical grasses, C3 plants endure in a cooler climate, such as grasses, shrubs and trees. CAM plants are mainly succulents (Cerling et al., 1993; Huang et al., 2001; Millard et al., 2008). The carbon isotope composition ($\delta^{13}C$) differs when plants use different pathways during photosynthesis. The $\delta^{13}C$ of C3-plants varies from about -23 to -35‰, averaging around -26‰ while the $\delta^{13}C$ of C4-plants is about -10 to -14‰, averaging around -13‰ (Cerling et al., 1993). Ratios of C3-C4 can be used to trace glacial-interglacial cycles; C4 photosynthesis is favored over C3 photosynthesis when there are low concentrations of carbon dioxide in the atmosphere (Huang et al., 2001; Millard et al., 2008). Also, the $\delta^{13}C$ within C3 plants is known to correlate with humidity; with increase in humidity, the incorporated $\delta^{13}C$ decreases about 2-7‰ (Winter et al., 1982). Thus, with the surficial variation of vegetation type, the signal in the soil can change, changing the isotopic composition of the meteoric water as well (Frappier et al., 2002). Deforestation occurred only after arrival of the first inhabitants which is why this signal is not visible in the carbon isotope record of the stalagmite. Although current vegetation cover suggests that the surface was more heavily vegetated before human settlement, British colonists mentioned that at the time of their settlement on Rodrigues around 1800, the western part of the island was mostly grass and small trees (Middleton and Burney, 2013).

Also, the age of the soil influences the $\delta^{13}C$; as the age of the soil increases, the $\delta^{13}C$ will increase. Therefore, when soil thickness exceeds 20 cm, a general top-bottom increase of 1-3‰ occurs (Stout et al., 1981). Thus, variability in soil thickness will alter meteoric water before percolating into the cave.

Lastly, humidity and temperature alter soil respiration rates (Boutton et al., 1998; Liu et al., 2017). The amount of old soil formation is temperature dependent because of correlation with soil respiration rates (Genty et al., 2001). Since vegetation cover change might not have had a large influence (see above) and little incorporated organic material input implies a thin soil cover, the dominant factor causing $\delta^{13}C$ variability is changes in soil respiration by change in humidity and or temperature. Thus, additionally to the calcium decrease, the two dips in the $\delta^{13}C$ trend seem to imply a period of increased humidity and elevated temperatures by altering the overlying soil on the cave (Genty et al., 2001).

4.3.3. Pathway

As the water seeps through the karst formation, one should consider the percolation time since it can result in a lag between forcing and the trend found in the stalagmite. The Mg/Ca and Sr/Ca content seem to be controlled by residence time, which refers in this case to the time it takes for the water to percolate through the soil into the cave. The longer the percolating time, the more calcite precipitation occurs along the flow path prior to precipitation

on the speleothems. This process is also referred to as prior calcite precipitation (PCP) (Genty et al., 2001). This increases the Mg and Sr content in the drip water, and decreases Ca along with an increase in $\delta^{13}C$. Thus, the percolation time in combination with speleothem growth rate influences the isotope value of the stalagmite. (van Breukelen, 2009; Genty et al., 2001). Some research suggests the correlation between partitioning of Mg in calcite speleothems with temperature, while others pose contradicting data (Verheyden, 2004). However, magnesium is below detection level in this speleothem, implying either a fast percolation time or low Mg content in the source carbonates. One period of increase in strontium is found around 1975-1875 BP, figure 10. However, this trend does coincide with a decrease in $\delta^{13}C$, figure 10. Since volcanic rock has high levels of strontium, increase in strontium content can also be explained by incorporation of volcanic rock due to increase in humidity. Why this trend is not visible in the first dip around 1375-1275 BP is not clear. Another trace element reflecting seepage throughflow is barium (Hellstrom and McCulloch, 2000). If $\delta^{13}C$ is negatively correlated with Ba (high $\delta^{13}C$, low Ba) a slower throughflow causes PCP, which can be linked to environmental humidity (Avalon et al., 1999; Hellstrom and McCulloch, 2000). Also, temperature related correlations were found by Goede (1994) in combination with a negative Br trend (Verheyden, 2004). However, there is not a trend visible in barium content since values are below detection level, like magnesium. The elements that do indicate changes in throughflow are calcium and strontium. These elements indicate that milky-white intervals are periods of increased throughflow, which might have changed the growth rate of the speleothem as well.

4.3.4. Internal

When the meteoric water has seeped through the karst formation, internal variability can still alter the final isotopic composition in the speleothem. For example, the pH of the drip water alters the dissolution ability of the carbonate rock (Hendy, 1971). The pH of the drip water decreases with the dissolution of $CaCO_3$, forming bicarbonate (HCO_3^-). Periods with an increase in precipitation can lead to a drop in pH due to increased dissolution of source carbonate. $\delta^{13}C$ in the drip water is unknown so this effect cannot be quantified. However, this effect was assumed to be negligible in the $\delta^{13}C$ variability of comparable speleothems (Frappier, 2002).

Other internal variability in $\delta^{13}C$ comes from the composition of stalagmite bands. Precipitated bands with higher organic content have lower $\delta^{13}C$ values than bands consistent of mostly limestone (Lauritzen and Lundberg, 1999). The input of organic material does not only correlate with the vegetation on top, also soil formation and relative limestone dissolution. However, the organic content of this stalagmite is rather low. This is reflected by the undetectably low aluminum concentrations in the stalagmite which also show no trend in the spectral analysis, and the color of the stalagmite (van Breukelen, 2009).

The growth rate of stalagmites is dependent on the Ca^{2+} content (Genty et al., 2001). Figure 8 showed a decrease of calcium in the milky layers which therefore likely had a higher growth rate than the more transparent layers. The higher growth rate sealed off the micropores in the structure rather than filling them with new carbonate minerals, resulting in bands with high fluid inclusion density (McDermott et al., 2006). Therefore, the alternation of milky and transparent layers is usually characterized by a sharp change in growth rate of the speleothem (McDermott et al., 2006). Due to the limited age model, hiatuses cannot be detected. However, it should be taken into consideration when looking at cyclicity in the records.

The last influence which may cause internal variability before locking the final isotope value in the stalagmite, is the rate of degassing. As drip water falls on the stalagmite, CO_2 degasses and $CaCO_3$ as explained in section 4.1. The faster the degassing, the less kinetic fractionation can alter the final $\delta^{13}C$ value (Lauritzen and Lundberg, 1999). As mentioned above, the Henry test gave insight in the degree at which the degassing rate influenced the precipitation process. The results suggest that there was no significant fractionation at moment of deposition in the transparent layers and little fractionation in the milky-white layers. However, there is currently discussion about the validity of the Hendy test (Dorale and Liu, 2009; Kluge and Affek, 2012; Meckler et al., 2014), because the test assumes that $\delta^{13}C$ is not affected by climate and that therefore carbon and oxygen isotopes behave independently. However, now it is known that $\delta^{13}C$ is affected by climate, just in a different way than $\delta^{18}O$ (Dorale and Liu, 2009). The concentration of CO_2 in the cave also influences the degassing rate: with low pCO_2 concentration, the degassing will be high.

4.4. Clumped isotope results

The isotope values were similar to values measured with the KIEL in Utrecht. However, the clumped isotope values had large deviation and had typical higher values than today's temperatures and the temperatures calculated with the formula by Lachniet [2014] using fluid inclusions measured by Spliethoff [2015]. Reasons for bias in the clumped isotope thermometry can be categorized into measurement errors and calibration errors.

4.4.1. Measurement errors

The to be measured values are relatively small, resulting in larger mass-spectrometer induced artifacts. Correction for this bias is critical for the final result: temperature. Additionally, the number of aliquots can be too little to get a precise value. Therefore, the first sample will be less accurate than the other samples. Because of the large number of aliquots needed, the sample size of the clumped isotopes is larger (± 4 mg) compared to samples in the GASBENCH (± 40 µg). Bigger sample sizes result in more precise measurements since bias can be corrected for by aliquots. A bigger sample size does lead to an average temperature signal

over a longer time. Also, the KIEL was stopped during the second run to switch bearings. Since the KIEL corrects the measured values with all previously measured standards, the correction was less precise after the switch.

4.4.2. Calibration errors

Meckler et al. [2014] found that the travertine calibration by Kele et al. [2015] led to a temperature bias of around 5 °C higher on average than the calibration posed by Meckler et al. [2014]. A possible reason is the faster precipitation rate of travertines versus synthesized calcite (which is used for the Meckler et al. [2014] calibration. Furthermore, this study found that clumped isotope temperatures were characterized with larger bias and variations with the Kele et al. [2015]. This paper concludes that the formula made from assessment at Leeds University conducts more precise temperatures. The same conclusion can be drawn from this thesis, see table 4. Furthermore, the assumption the speleothem was 100% aragonite was based on XRF data. This could be incorrect as well. Changing the crystallography assumption will lead to a different correction for the clumped results. The assumption on crystallography was based on a research by Perrin et al. [2014]. Contradicting research by Turgeon and Lundberg [2001] states that the Mg/Ca in aragonites should be >2.9 and that most calcites consist of low Mg values. A reason for the low Mg content in the speleothem, is that it was not present in the drip water and therefore not in the source carbonates as well. However, the Mg and Sr content is dependent on the drip water. A source of Sr can be volcanic leaching. Drip water content and partition coefficients between Mg, Sr and Ca are needed over time is needed to ensure this statement.

When assuming all aliquots having the same temperature, the average temperature can be calculated (table 4). The temperature was 39.2 °C according to the Kele [2014] calibration and Kele et al. [2015] found an offset of about 10 °C in some samples. Taking this into account, the value can be accurate though relatively imprecise; measurement validity remains low for the clumped isotopes. One should be careful drawing conclusions from these measurements.

4.5. Paleo-climatological reconstruction

The isotope records suggest a linear increasing desiccation trend between 2750-1200 years BP, so during the lifespan of this stalagmite. Two periods of sharp increase in humidity are indicated in the carbon isotope record around 1975-1875 BP and 1375-1275 BP. This section will put the results into a bigger climatological perspective. Clumped isotopes and fluid inclusion data showed relatively stable temperatures between 25-30 °C, which agrees with the subtropical climate temperature range.

From the Holocene Climatic Optimum (HCO) occurring in the Early Holocene on to the Mid-Holocene to today, a shift from a humid and warm period to a long-term cooling and

drying was observed within several climate records, including lake sediments and ice cores (Kilimanjaro) on the Southern Hemisphere (Conroy et al., 2008; Claussen et al., 1999; Lee-Thorp et al., 2001; Liu et al., 2014; Thompson et al., 2002; Abram, 2007). The warm and humid period in Africa was characterized by ubiquitous presence of lakes and vegetation and is called the African Humid Period (AHP), a period from about 11.5 to 5.5 kyr. cal. BP (Renssen et al., (2006). Insolation changes over the Holocene are mainly driven by Milankovitch precession cycle. The timing of the HCO correlates with a precession maximum. After 8000 kyr. BP, the precession cycle drives incoming solar radiation, decreasing seasonality on the Southern Hemisphere while increasing seasonality on the Northern Hemisphere (Haug, 2001; Shanahan et al., 2015). After the HCO, desertification of the Saharan and Arabian area occurred (Claussen et al., 1999; Marriner et al., 2012; Renssen et al., 2006). This resulted in a southward biome shift on the African continent and a change in precipitation patterns (Marcott et al., 2013; Shevenell et al., 2011; Truc et al., 2013; Shanahan et al., 2015; Wei and Wang, 2004; Wolfe et al., 2001). There are several carbonate and sediment records indicating a change in temperature and humidity on the Southern Hemisphere as well (Gingele, 1996; Lee-Thorp et al., 2001).

However, if precipitation is driven by orbital forcing shifting the ICTZ, it is expected that Southern and Northern climate records are not in phase (Haug, 2001). However, previous research on the African continent suggest that interannual variability of SST in the Indian Ocean plays a dominant role, where the Indian monsoon on the Northern Hemisphere determines precipitation patterns on the African continent (Tierney et al., 2008).

4.5.1. Indian Ocean Dipole

Based on a sediment record from Mauritius Island and coral records, De Boer et al. [2014] suggested a shift from a more positive IOD to a more negative IOD state from the Middle-Holocene on. Short decadal-scale positive IOD events occurred within this 350-year cyclicity. This cyclicity is also visible in the stalagmite record from La Vierge, as shown in the wavelet analysis, figure 16 and 17. Small-scale cyclicity is visible in the strontium record (figure 8 and 12). However, this cyclicity can also be caused by ENSO.

4.5.2. El Niño–Southern Oscillation

The two dips in the $\delta^{13}C$ record, 1375-1275 BP and 1975-1875 BP, can be marked as relatively humid, this can also be seen in the milky-white, low density, layers (Bar-Matthews et al., 1996; McDermott et al., 2006). A period of increased humidity can be caused by a strong El Niño event, leading to a decrease in the throughflow of Indonesian warmer waters, forcing the system to a positive IOD state. Along with the increasing SST in the eastern Indian ocean, the location of the Mascarene high will shift zonally, in this case eastward (Manatsa et al., 2004) leading to more and longer rain events in East-Africa. Connection between the IOD and the El Niño–Southern Oscillation (ENSO) has been recognized, though scientists have not yet

come to a consensus (Muangsong et al., 2014, Saji et al., 1999; Behera et al., 2006; Fischer et al., 2005; De Boer et al., 2014). In figure 27, a correlation between El Niño events and the $\delta^{13}C$ is illustrated. The dip around 1300 BP does show co-occurrence of increased El Niño events.

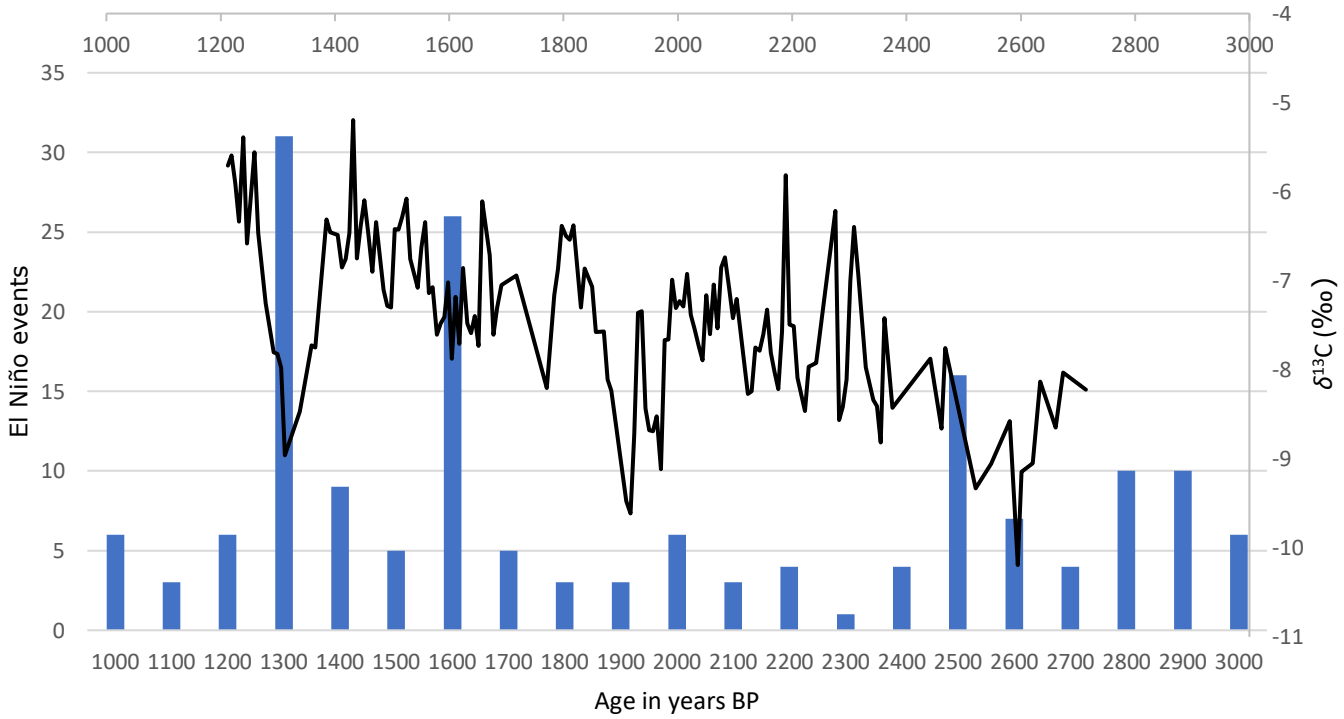

Figure 27. Combined chart of the $\delta^{13}C$ record (black line) from the La Vierge stalagmite and El Niño events (blue bars. El Niño events data presented by Moy et al. [2002].

The El Niño event chart in figure 27 is based on a 6-meter long sediment core from lake Laguna Pallcacocha (Peru) near the western Pacific, correlating El Niño to occurring flood events from Moy et al. [2002]. Other records show a trend in El Niño events over the Holocene; for example, Rein et al. [2004] shows a strong shift from a high El Niño intensity before 1250 BP to a weaker El Niño in the Medieval warm period.

4.5.3. Pacific Decadal Oscillation

Significant cyclicity in the oxygen and carbon record had a decadal scale (figure 14/15 and figure 19/20). In the wavelet analysis (figure 16 and 17) variation in significant cyclicity is visible. The decadal cyclicity has alternating periods of dominance.

Possible explanation can be found within the precipitation and SST patterns and anomalies of the Pacific Ocean (Mantua and Hare, 2002). Barron and Anderson [2011] presented PDO mode shifts over the Holocene period from two lake sediment records from North America. These records showed alternating dominating positive or negative PDO modes.

Around 1200 BP there was a shift from a more dominant negative PDO mode to a more positive mode, which could have induced stronger and more El Niño events as shown in figure 24 (Newman et al., 2003).

From this data, the dominant climatological driver would be the PDO, but it should be noted that yearly cyclicity may not have been detected because of inadequate sample density. Still, decadal cyclicity is significant. Which climatological driver is dominant cannot be determined from this data. However, the yearly cyclicity is visible in the strontium and calcium content of the stalagmite. This could be reassuring that although yearly cyclicity was not visible in the isotope records, it was simply undetected due to insufficient sample density. Either smaller sample sizes or the usage of a faster growing speleothem may resolve this insufficient sample density. It can be speculated that when ENSO and PDO are working together, they can force the Indian Ocean system into a mode shift. In this case leading to a period of increased humidity. Thus, careful conclusions should be drawn about the intercorrelation between climatological drivers in the Southwestern Indian Ocean in the Late Holocene.

4.6. Comparison to previous research

The presented record can be compared with a stalagmite from the same cave analyzed by Rijsdijk et al. [2011]. One would expect that speleothems in the same cave have the same isotopic signals (Feng et al., 2014; van Breukelen, 2009). The Rijsdijk et al. [2011] record has a comparable range in the $\delta^{18}O$ data from the La Vierge stalagmite. Also, both records have an increasing trend in $\delta^{13}C$. The $\delta^{13}C$ in the Rijsdijk stalagmite have lower values overall compared to the $\delta^{13}C$ record presented in this thesis. However, the Rijsdijk et al. [2011] record extends further back in time (4200-2250 cal. yr. BP) than the record here presented. Combining the two records, the trend of desiccation of the Rodrigues area can be traced even further back in time. Rijsdijk et al. [2011] linked $\delta^{18}O$ cyclicity (among others) to the mass-extinction of several species in Mauritius, including Dodo birds (Raphus cucullatus) and giant tortoises (Cylindraspis spp.) due to the lowering of ground water level. Therefore, results of this thesis might also be correlated with the local biodiversity and hydrology on the island. Further research in the extent of this correlation might ascertain this hypothesis.

Research by Li et al. [2016] (unpublished) on a La Vierge stalagmite covering the period of 11,000-300 years cal. yr. BP showed comparable linear trends in the carbon and oxygen isotopes. According to the Replication Test, proposed by Dorale and Liu [2009], isotopic equilibrium during precipitation in this speleothem is likely to have occurred. This supports the validity of the results presented in this thesis.

In the future, it is predicted that the Indian Ocean will take up more heat (Roxy et al., 2014; Lee et al., 2015). The trend over the last decades was the cooling of the Pacific Ocean with

the additional storage in the Indian Ocean due to increasing transport of warm waters into the Indian Ocean (Lee et al., 2015). The ITF will increase, which will shift the Mascarene High westward. Therefore, it is expected that with global warming, aridity over the Rodrigues Island region will increase.

Conclusion

Several methods were applied on a speleothem to reconstruct and find the dominant climatological drivers of SST variability in the Southeastern Indian Ocean. These methods are X-ray, UV-radiation, isotope analysis and clumped isotope thermometry. An 11-centimeter long stalagmite was used from the La Vierge cave in Rodrigues Island, located in the Western Indian Ocean. The stalagmite covered a period of 1550 years from 2700-1200 BP.

In the stalagmite, alternation between growth bands was visible under X-ray and UV-radiation. The stalagmite consisted of alternating intervals between milky-white and transparent bands. XRF-scans showed correlation between the intervals and calcium content. Lower calcium and higher strontium content was visible in the milky-white intervals caused by leaching of minerals. Volcanic rock can be a possible source of strontium leaching. Thus, milky-white layers correspond to relatively humid intervals and the transition between milky-white and transparent layers will mark a change in growth rate.

The isotope record showed a linear increasing trend in both the carbon ($\delta^{13}C$) and oxygen ($\delta^{18}O$) isotopes. These increasing carbon and oxygen isotope values were interpreted as increasing aridity over this period in a cooling climate. This agrees with the general cooling trend after the African Humid Period (AHP) around 11.5 to 5.5 kyr. cal. BP. The trend in the Indian Ocean climatology agrees with the positive radiative forcing Northern Hemisphere which resulted in the Holocene Climatic Optimum (HCO) (Fleitmann et al., 2007). Two dips in the $\delta^{13}C$ around 1975-1875 BP and 1375-1275 BP can be linked to milky-white intervals. The dominant variable for these dips is increased soil respiration, which can be interpreted as periods of increased precipitation and/or humidity in the area. The dominant variable in $\delta^{18}O$ is the amount effect, which has a less regional character and showed larger scatter in the results.

Clumped isotope thermometry and XRF-scans were used to support the isotope records and to filter the signal from the different variables causing climatological variability. Paleotemperatures were determined with clumped isotope thermometry using calibrations of Meckler [2014] and Kele [2015]. The Meckler [2014] calibration had more reliable results, with temperatures around 30°C. It can therefore be concluded that the methods used on the speleothem proxy seemed to support each other and agree with other records in the area even though measurement validity was different per method.

Thus, with the findings in this thesis, the general research question can be answered. Answers to the sub-research questions will aid the conclusions.

- Which cyclicities are present and dominant in the speleothem record?

REDFIT spectral analysis and wavelet analysis showed different dominant cyclicities in the strontium content and in the carbon and oxygen isotopes. The strontium record had a yearly, as well as a centennial scale cyclicity. The carbon and oxygen isotopes showed a dominant decadal cyclicity.

- How are the cyclicities interconnected in the speleothem record?

The yearly and decadal cyclicity in temperature and humidity could be the effect of interconnection between IOD, ENSO and PDO. ENSO and PDO are connected to the IOD through the ITF. The interplay between these climatological phenomena regulates SST and SSP. This interplay drives atmospheric circulation and precipitation in the Rodrigues area. ENSO seems to be driving the IOD state. The PDO in turn is driving the strength of ENSO. Other interpretation is given by De Boer et al. [2014]. They interpreted the data as a 350-year interval with decadal-scale positive IOD events.

- What is the regional and global pattern when the data is extrapolated?

Precipitation variability on Rodrigues Island is correlated to the location of the Mascarene High and Intertropical Convergence Zone. Comparing the data from this thesis to data from Li et al [unpublished] and Rijsdijk et al. [2011] from the same cave, showed that isotope values and trends are similar. This supports the measurement validity as well as the internal validity of this thesis. When combining the isotope records, the trend in desiccation can be extended even further towards the HCO, which ended about 5000 years BP. Centennial as well as yearly scale cyclicity was also found by the Boer et al. [2014]. It is expected that due to global warming, heat uptake by the Indian Ocean will increase (Roxy et al., 2014; Lee et al., 2015) leading to increased drought in the Rodrigues Island area.

Which climatological drivers were dominant in the Late Holocene causing SST variability in the subtropical Indian Ocean?

Lastly, to answer the general research question: in this thesis, several climatological drivers in the subtropical Indian Ocean could be specified. However, because external validity cannot be fully accounted for, intercorrelation between them remains open for debate.

Acknowledgements

In this part I would like to thank everyone that helped me in my process of executing this research and gave me the ability to do so. First, I would like to thank Hubert Vonhof, who gave me the opportunity to work with the stalagmite, who assisted and supervised me during my isotope analysis in Mainz and started the first discussion of the results. Secondly, I would like to thank Rick Hennekam, who helped me taking the first and the last steps. I would like to thank Martin Ziegler, who helped interpreting the clumped isotope data and Gert-Jan Reichart for supervising the whole project. Lastly, I would like to thank my parents, Job van Merode and Stan Frambach who were motivational pillars preventing the project from falling and helped me finalize my thesis.

References

Abram, N. J., Gagan, M. K., Liu, Z., Hantoro, W. S., McCulloch, M. T., & Suwargadi, B. W. (2007). Seasonal characteristics of the Indian Ocean Dipole during the Holocene epoch. *Nature*, *445*(7125), 299-302.

Abram, N. J., Gagan, M. K., Cole, J. E., Hantoro, W. S., & Mudelsee, M. (2008). Recent intensification of tropical climate variability in the Indian Ocean. *Nature Geoscience*, 1(12), 849-853.

Allen, J. (1977). Short term spectral analysis, synthesis, and modification by discrete Fourier transform. *IEEE Transactions on Acoustics, Speech, and Signal Processing*, *25*(3), 235-238.

Ayalon, A., Bar-Matthews, M., & Kaufman, A. (1999). Petrography, strontium, barium and uranium concentrations, and strontium and uranium isotope ratios in speleothems as paleoclimatic proxies: Soreq Cave, Israel. *The Holocene*, *9*(6), 715-722.

Baker, A., Smart, P. L., Edwards, R. L., & Richards, D. A. (1993). Annual growth banding in a cave stalagmite. *Nature*, *364*(6437), 518-520.

Baker, A., Barnes, W. L., & Smart, P. L. (1996). Speleothem luminescence intensity and spectral characteristics: Signal calibration and a record of paleo-vegetation change. *Chemical Geology*, *130*(1-2), 65-76.

Bar-Matthews, M., Ayalon, A., Matthews, A., Sass, E., & Halicz, L. (1996). Carbon and oxygen isotope study of the active water-carbonate system in a karstic Mediterranean cave: Implications for paleoclimate research in semiarid regions. *Geochimica et Cosmochimica Acta*, *60*(2), 337-347.

Behera, S. K., Luo, J. J., Masson, S., Rao, S. A., Sakuma, H., & Yamagata, T. (2006). A CGCM study on the interaction between IOD and ENSO. *Journal of Climate*, *19*(9), 1688-1705.

Bögli, A. (2012). *Karst hydrology and physical speleology*. Springer Science & Business Media.

Böhm, F., Haase-Schramm, A., Eisenhauer, A., Dullo, W. C., Joachimski, M. M., Lehnert, H., & Reitner, J. (2002). Evidence for preindustrial variations in the marine surface water carbonate system from coralline sponges. *Geochemistry, Geophysics, Geosystems*, *3*(3), 1-13.

Baudoin, M. A., Vogel, C., Nortje, K., & Naik, M. (2017). Living with drought in South Africa: lessons learnt from the recent El Niño drought period. *International Journal of Disaster Risk Reduction*, *23*, 128-137.

De Boer, E. J., Tjallingii, R., Vélez, M. I., Rijsdijk, K. F., Vlug, A., Reichart, G. J., ... & Hooghiemstra, H. (2014). Climate variability in the SW Indian Ocean from an 8000-yr long multi-proxy record in the Mauritian lowlands shows a middle to late Holocene shift from negative IOD-state to ENSO-state. *Quaternary Science Reviews*, *86*, 175-189.

Bousquet, P., Peylin, P., Ciais, P., Le Quéré, C., Friedlingstein, P., & Tans, P. P. (2000). Regional changes in carbon dioxide fluxes of land and oceans since 1980. *Science*, *290*(5495), 1342-1346.

Boutton, T. W., Archer, S. R., Midwood, A. J., Zitzer, S. F., & Bol, R. (1998). δ 13 C values of soil organic carbon and their use in documenting vegetation change in a subtropical savanna ecosystem. *Geoderma*, *82*(1), 5-41.

Breitenbach, S. F., & Bernasconi, S. M. (2011). Carbon and oxygen isotope analysis of small carbonate samples (20 to 100 µg) with a GasBench II preparation device. *Rapid Communications in Mass Spectrometry*, *25*(13), 1910-1914.

Bryden, H. L., Beal, L. M., & Duncan, L. M. (2005). Structure and transport of the Agulhas Current and its temporal variability. *Journal of Oceanography*, *61*(3), 479-492.

Burney, D. A., Hume, J. P., Middleton, G. J., Steel, L., Burney, L. P., & Porch, N. (2015). Stratigraphy and chronology of karst features on Rodrigues Island, Southwestern Indian Ocean. *Journal of Cave and Karst Studies*, 77(1), 37.

van Breukelen, M. R. (2009). Peruvian stalagmites as archives of Holocene temperature and rainfall variability.

Cai, W., Borlace, S., Lengaigne, M., Van Rensch, P., Collins, M., Vecchi, G., ... & England, M. H. (2014). Increasing frequency of extreme El Niño events due to greenhouse warming. *Nature climate change, 4*(2), 111-116.

Cassimally, Y. (2015) Digest of statistics on Rodrigues, published July 2016.

Cerling, T. E., Wang, Y., & Quade, J. (1993). Expansion of C4 ecosystems as an indicator of global ecological change in the late Miocene. *Nature*, *361*(6410), 344-345.

Claussen, M., Kubatzki, C., Brovkin, V., Ganopolski, A., Hoelzmann, P., & Pachur, H. J. (1999). Simulation of an abrupt change in Saharan vegetation in the Mid-Holocene. *Geophysical research letters*, *26*(14), 2037-2040.

Conroy, J. L., Overpeck, J. T., Cole, J. E., Shanahan, T. M., & Steinitz-Kannan, M. (2008). Holocene changes in eastern tropical Pacific climate inferred from a Galápagos lake sediment record. *Quaternary Science Reviews*, *27*(11), 1166-1180.

Currie, J. C., Lengaigne, M., Vialard, J., Kaplan, D. M., Aumont, O., Naqvi, S. W. A., & Maury, O. (2013). Indian Ocean Dipole and El Niño/Southern Oscillation impacts on regional chlorophyll anomalies in the Indian Ocean.

Dansgaard, W. (1964). Stable isotopes in precipitation. *Tellus, 16*(4), 436-468.

Dandurand, G., Maire, R., Ortega, R., Devès, G., Lans, B., Morel, L., ... & Billy, I. (2011). X-ray fluorescence microchemical analysis and autoradiography applied to cave deposits: speleothems, detrital rhythmites, ice and prehistoric paintings. *Géomorphologie: relief, processus, environnement*, *17*(4), 407-426.

Dorale, J. A., & Liu, Z. (2009). Limitations of Hendy test criteria in judging the paleoclimatic suitability of speleothems and the need for replication. *Journal of Cave and Karst Studies*, *71*(1), 73-80.

Douglas, P. M., Affek, H. P., Ivany, L. C., Houben, A. J., Sijp, W. P., Sluijs, A., ... & Pagani, M. (2014). Pronounced zonal heterogeneity in Eocene southern high-latitude sea surface temperatures. *Proceedings of the National Academy of Sciences*, *111*(18), 6582-6587.

Douville, E., Sallé, E., Frank, N., Eisele, M., Pons-Branchu, E., & Ayrault, S. (2010). Rapid and accurate U–Th dating of ancient carbonates using inductively coupled plasma-quadrupole mass spectrometry. *Chemical Geology*, *272*(1), 1-11.

Eiler, J. M. (2011). Paleoclimate reconstruction using carbonate clumped isotope thermometry. *Quaternary Science Reviews, 30*(25), 3575-3588.

Fischer, A. S., Terray, P., Guilyardi, E., Gualdi, S., & Delecluse, P. (2005). Two independent triggers for the Indian Ocean dipole/zonal mode in a coupled GCM. *Journal of climate*, *18*(17), 3428-3449.

Fleitmann, D., Burns, S. J., Mudelsee, M., Neff, U., Kramers, J., Mangini, A., & Matter, A. (2003). Holocene forcing of the Indian monsoon recorded in a stalagmite from southern Oman. *Science, 300*(5626), 1737-1739.

Fleitmann, D., Burns, S. J., Mangini, A., Mudelsee, M., Kramers, J., Villa, I., ... & Matter, A. (2007). Holocene ITCZ and Indian monsoon dynamics recorded in stalagmites from Oman and Yemen (Socotra). *Quaternary Science Reviews*, *26*(1), 170-188.

Folk, R. L., & Land, L. S. (1975). Mg/Ca ratio and salinity: two controls over crystallization of dolomite. *AAPG bulletin*, *59*(1), 60-68.

Frappier, A., Sahagian, D., González, L. A., & Carpenter, S. J. (2002). El Nino events recorded by stalagmite carbon isotopes. *Science*, *298*(5593), 565-565.

Frisia, S. (1996). TEM and SEM investigation of speleothem carbonates: another key to the interpretation of environmental parameters. *Climate Change: The Karst Record: Karst Water Institute, Special Publication*, *2*, 33-34.

Frisia, S., Borsato, A., Fairchild, I. J., & McDermott, F. (2000). Calcite fabrics, growth mechanisms, and environments of formation in speleothems from the Italian Alps and southwestern Ireland. *Journal of Sedimentary Research*, *70*(5), 1183-1196.

Frisia, S., Borsato, A., Fairchild, I. J., & Susini, J. (2005). Variations in atmospheric sulphate recorded in stalagmites by synchrotron micro-XRF and XANES analyses. *Earth and Planetary Science Letters*, *235*(3), 729-740.

Funk, C., Dettinger, M. D., Michaelsen, J. C., Verdin, J. P., Brown, M. E., Barlow, M., & Hoell, A. (2008). Warming of the Indian Ocean threatens eastern and southern African food security but could be mitigated by agricultural development. *Proceedings of the national academy of sciences, 105*(32), 11081-11086.

Gade, D. W. (1985). Man, and nature on Rodrigues: tragedy of an island common. *Environmental Conservation*, *12*(03), 207-216.

Garrels, R. M., & Christ, C. L. (1965). Solutions, minerals, and equilibria.

Geiger, Rudolf (1954). "Klassifikation der Klimate nach W. Köppen" [Classification of climates after W. Köppen]. *Landolt-Börnstein – Zahlenwerte und Funktionen aus Physik, Chemie, Astronomie, Geophysik und Technik, alte Serie*. Berlin: Springer. **3**. pp. 603–607.

Genty, D., Baker, A., Massault, M., Proctor, C., Gilmour, M., Pons-Branchu, E., & Hamelin, B. (2001). Dead carbon in stalagmites: carbonate bedrock paleodissolution vs. ageing of soil organic matter. Implications for 13 C variations in speleothems. *Geochimica et Cosmochimica Acta*, *65*(20), 3443-3457.

Genty, D., Baker, A., & Vokal, B. (2001). Intra-and inter-annual growth rate of modern stalagmites. *Chemical Geology*, *176*(1), 191-212.

Genty, D., Blamart, D., Ouahdi, R., Gilmour, M., Baker, A., Jouzel, J., & Van-Exter, S. (2003). Precise dating of Dansgaard–Oeschger climate oscillations in western Europe from stalagmite data. *Nature*, *421*(6925), 833-837.

Gingele, F. X. (1996). Holocene climatic optimum in Southwest Africa—evidence from the marine clay mineral record. *Palaeogeography, Palaeoclimatology, Palaeoecology*, *122*(1-4), 77-87.

Grant, K. M., Rohling, E. J., Bar-Matthews, M., Ayalon, A., Medina-Elizalde, M., Ramsey, C. B., ... & Roberts, A. P. (2012). Rapid coupling between ice volume and polar temperature over the past 150,000 [thinsp] years. *Nature*, *491*(7426), 744-747.

Grossman, E. L., & Ku, T. L. (1986). Oxygen and carbon isotope fractionation in biogenic aragonite: temperature effects. *Chemical Geology: Isotope Geoscience section*, *59*, 59-74.

Hammer, Ø., Harper, D. A. T., & Ryan, P. D. (2001). Paleontological Statistics (PAST) 2.06.

He, B., Olack, G. A., & Colman, A. S. (2012). Pressure baseline correction and high-precision CO2 clumped-isotope (Δ 47) measurements in bellows and micro-volume modes. *Rapid Communications in Mass Spectrometry*, *26*(24), 2837-2853.

Hendy, C. H. (1971). The isotopic geochemistry of speleothems—I. The calculation of the effects of different modes of formation on the isotopic composition of speleothems and their applicability as palaeoclimatic indicators. *Geochimica et cosmochimica Acta*, *35*(8), 801-824.

Hilkert, W., & Havak, H. (2016). Isotope analysis of water, fruit juice and wine using the Thermo Scientific GasBench II IRMS. Thermo Fischer Scientific, Bremen, Germany.

Huang, Y. A., Street-Perrott, F. A., Metcalfe, S. E., Brenner, M., Moreland, M., & Freeman, K. H. (2001). Climate change as the dominant control on glacial-interglacial variations in C3 and C4 plant abundance. *Science*, *293*(5535), 1647-1651.

Hunter, R. S. (1942). Photoelectric tristimulus colorimetry with three filters. *JOSA*, *32*(9), 509-538.

Huntington, K. W., Eiler, J. M., Affek, H. P., Guo, W., Bonifacie, M., Yeung, L. Y., ... & Came, R. (2009). Methods and limitations of 'clumped' CO_2 isotope (Δ47) analysis by gas-source isotope ratio mass spectrometry. *Journal of Mass Spectrometry, 44(9)*, 1318-1329.

IAEA (2001). GNIP Maps and Animations, International Atomic Energy Agency, Vienna. Accessible at http://isohis.iaea.org.

Kele, S., Breitenbach, S. F., Capezzuoli, E., Meckler, A. N., Ziegler, M., Millan, I. M., ... & Yan, H. (2015). Temperature dependence of oxygen-and clumped isotope fractionation in carbonates: A study of travertines and tufas in the 6–95 C temperature range. *Geochimica et Cosmochimica Acta*, *168*, 172-192.

Kendall, A. C., & Broughton, P. L. (1978). Origin of fabrics in speleothems composed of columnar calcite crystals. *Journal of Sedimentary Research*, *48*(2).

Kluge, T., Marx, T., Scholz, D., Niggemann, S., Mangini, A., & Aeschbach-Hertig, W. (2008). A new tool for paleoclimate reconstruction: Noble gas temperatures from fluid inclusions in speleothems. *Earth and Planetary Science Letters*, *269*(3), 408-415.

Kluge, T., & Affek, H. P. (2012). Quantifying kinetic fractionation in Bunker Cave speleothems using Δ 47. *Quaternary Science Reviews*, *49*, 82-94.

Kotlia, B. S., Ahmad, S. M., Zhao, J. X., Raza, W., Collerson, K. D., Joshi, L. M., & Sanwal, J. (2012). Climatic fluctuations during the LIA and post-LIA in the Kumaun Lesser Himalaya, India: Evidence from a 400-year old stalagmite record. *Quaternary International*, *263*, 129-138.

Krishnan, R., & Sugi, M. (2003). Pacific decadal oscillation and variability of the Indian summer monsoon rainfall. *Climate Dynamics*, *21*(3-4), 233-242.

Krüger, Y., Marti, D., Staub, R. H., Fleitmann, D., & Frenz, M. (2011). Liquid–vapor homogenization of fluid inclusions in stalagmites: Evaluation of a new thermometer for paleoclimate research. *Chemical geology*, *289*(1), 39-47.

Kwiatkowski, C., Prange, M., Varma, V., Steinke, S., Hebbeln, D., & Mohtadi, M. (2015). Holocene variations of thermocline conditions in the eastern tropical Indian Ocean. *Quaternary Science Reviews*, *114*, 33-42.

Lace, M. J., & Mylroie, J. E. (Eds.). (2013). *Coastal karst landforms.* Springer Science & Business Media.

Lachniet, M. S. (2009). Climatic and environmental controls on speleothem oxygen-isotope values. *Quaternary Science Reviews, 28*(5), 412-432.

Lauritzen, S. E., & Lundberg, J. (1999). Speleothems and climate: a special issue of The Holocene. *The Holocene*, *9*(6), 643-647.

Lee, J. E., & Fung, I. (2008). "Amount effect" of water isotopes and quantitative analysis of post-condensation processes. *Hydrological Processes, 22*(1), 1-8.

Lee, S. K., Park, W., Baringer, M. O., Gordon, A. L., Huber, B., & Liu, Y. (2015). Pacific origin of the abrupt increase in Indian Ocean heat content during the warming hiatus. *Nature Geoscience, 8*(6), 445-449.

Lee-Thorp, J. A., Holmgren, K., Lauritzen, S. E., Linge, H., Moberg, A., Partridge, T. C., ... & Tyson, P. D. (2001). Rapid climate shifts in the southern African interior throughout the mid to late Holocene. *Geophysical Research Letters*, *28*(23), 4507-4510.

Linsley, B. K., Rosenthal, Y., & Oppo, D. W. (2010). Holocene evolution of the Indonesian throughflow and the western Pacific warm pool. *Nature Geoscience*, *3*(8), 578.

Liu, Z., Zhu, J., Rosenthal, Y., Zhang, X., Otto-Bliesner, B. L., Timmermann, A., ... & Timm, O. E. (2014). The Holocene temperature conundrum. *Proceedings of the National Academy of Sciences*, *111*(34), E3501-E3505.

Liu, Y., Oster, J. L., & Druhan, J. L. (2017). The hydrologic record of karst systems: linking soil moisture to the carbon isotope signatures of soils above the Blue Spring cave system. *Acta Geochimica*, 1-4.

Lutjeharms, J. R., & Bornman, T. G. (2010). The importance of the greater Agulhas Current is increasingly being recognized. *South African Journal of Science*, *106*(3-4), 1-4.

Mallick, R., & Frank, N. (2002). A new technique for precise uranium-series dating of travertine micro-samples. *Geochimica et Cosmochimica Acta*, *66*(24), 4261-4272.

Mantua, N. J., & Hare, S. R. (2002). The Pacific decadal oscillation. *Journal of oceanography*, *58*(1), 35-44.

Marcott, S. A., Shakun, J. D., Clark, P. U., & Mix, A. C. (2013). A reconstruction of regional and global temperature for the past 11,300 years. *science*, *339*(6124), 1198-1201.

Marriner, N., Flaux, C., Kaniewski, D., Morhange, C., Leduc, G., Moron, V., ... & Stanley, J. D. (2012). ITCZ and ENSO-like pacing of Nile delta hydro-geomorphology during the Holocene. *Quaternary Science Reviews*, *45*, 73-84.

Meckler, A. N., Ziegler, M., Millán, M. I., Breitenbach, S. F., & Bernasconi, S. M. (2014). Long-term performance of the Kiel carbonate device with a new correction scheme for clumped isotope measurements. *Rapid Communications in Mass Spectrometry*, *28*(15), 1705-1715.

Meckler, A. N., Affolter, S., Dublyansky, Y. V., Krüger, Y., Vogel, N., Bernasconi, S. M., ... & Carolin, S. (2015). Glacial–interglacial temperature change in the tropical West Pacific: A comparison of stalagmite-based paleo-thermometers. *Quaternary Science Reviews*, *127*, 90-116.

McDermott, F. (2004). Paleo-climate reconstruction from stable isotope variations in speleothems: a review. *Quaternary Science Reviews, 23*(7), 901-918.

McDermott, F., Schwarcz, H., & Rowe, P. J. (2006). *Isotopes in speleothems* (pp. 185-225). Springer Netherlands Meehl, G. A., Arblaster, J. M., Fasullo, J. T., Hu, A., & Trenberth, K. E. (2011). Model-based evidence of deep-ocean heat uptake during surface-temperature hiatus periods. *Nature Climate Change*, *1*(7), 360-364.

Middleton, G. J., & Burney, D. A. (2013). Rodrigues–An Indian Ocean Island calcarenite: its history, study and management. In *Coastal Karst Landforms* (pp. 261-276). Springer Netherlands.

Millard, P., Midwood, A. J., Hunt, J. E., Whitehead, D., & Boutton, T. W. (2008). Partitioning soil surface CO 2 efflux into autotrophic and heterotrophic components, using natural gradients in soil δ 13 C in an undisturbed savannah soil. *Soil Biology and Biochemistry*, *40*(7), 1575-1582.

Moy, C. M., Seltzer, G. O., Rodbell, D. T., & Anderson, D. M. (2002). Variability of El Niño/Southern Oscillation activity at millennial timescales during the Holocene epoch. *Nature*, *420*(6912), 162-165.

Muangsong, C., Cai, B., Pumijumnong, N., Hu, C., & Cheng, H. (2014). An annually laminated stalagmite record of the changes in Thailand monsoon rainfall over the past 387 years and its relationship to IOD and ENSO. *Quaternary International*, 349, 90-97.

Mylroie, J. & Middleton, G. Carbonates Evaporites (2016) 31: 421. doi:10.1007/s13146-016-0299-0

Newman, M., Compo, G. P., & Alexander, M. A. (2003). ENSO-forced variability of the Pacific decadal oscillation. *Journal of Climate*, *16*(23), 3853-3857.

Pachauri, R. K., & Reisinger, A. (2007). IPCC fourth assessment report. *IPCC, Geneva*, 2007.

Paillard, D., Labeyrie, L., & Yiou, P. (1996). Macintosh program performs time-series analysis. *Eos, Transactions American Geophysical Union*, *77*(39), 379-379.

Perrin, C., Prestimonaco, L., Servelle, G., Tilhac, R., Maury, M., & Cabrol, P. (2014). Aragonite–calcite speleothems: identifying original and diagenetic features. *Journal of Sedimentary Research*, *84*(4), 245-269.

Rein, B., Lückge, A., & Sirocko, F. (2004). A major Holocene ENSO anomaly during the Medieval period. *Geophysical Research Letters*, *31*(17).

Renssen, H., Brovkin, V., Fichefet, T., & Goosse, H. (2006). Simulation of the Holocene climate evolution in Northern Africa: the termination of the African Humid Period. *Quaternary International*, *150*(1), 95-102.

Revesz, K. M., Landwehr, J. M., & Keybl, J. (2001). Measurement of delta13C and delta18O Isotopic Ratios of CaCO3 Using a Thermoquest Finnigan GasBench II Delta Plus XL Continuous Flow Isotope Ratio Mass Spectrometer with Application to Devils Hole Core DH-11 Calcite (No. USGS-01-257). *GEOLOGICAL SURVEY RESTON VA.*

Richter M. (2001). Vegetationszonen der Erde. Klett-Perthes, Gotha.

Rijsdijk, K. F., Zinke, J., de Louw, P. G., Hume, J. P., van der Plicht, H., Hooghiemstra, H., ... & Baider, C. (2011). Mid-Holocene (4200 kyr BP) mass mortalities in Mauritius (Mascarenes): Insular vertebrates resilient to climatic extremes but vulnerable to human impact. *The Holocene*, *21*(8), 1179-1194.

Roxy, M. K., Ritika, K., Terray, P., & Masson, S. (2014). The Curious Case of Indian Ocean Warming. *Journal of Climate*, 27(22), 8501-8509.

Saji, N. H., Goswami, B. N., Vinayachandran, P. N., & Yamagata, T. (1999). A dipole mode in the tropical Indian Ocean. *Nature, 401(6751*), 360-363.

Schmid, T. W., & Bernasconi, S. M. (2010). An automated method for 'clumped-isotope' measurements on small carbonate samples. *Rapid Communications in Mass Spectrometry*, *24*(14), 1955-1963.

Schneider, T., Bischoff, T., & Haug, G. H. (2014). Migrations and dynamics of the intertropical convergence zone. *Nature*, *513*(7516), 45.

Schulz, M., & Mudelsee, M. (2002). REDFIT: estimating red-noise spectra directly from unevenly spaced paleoclimatic time series. *Computers & Geosciences*, *28*(3), 421-426.

Shanahan, T. M., McKay, N. P., Hughen, K. A., Overpeck, J. T., Otto-Bliesner, B., Heil, C. W., ... & Peck, J. (2015). The time-transgressive termination of the African Humid Period. *Nature Geoscience*, *8*(2), 140.

Shapiro, S. S., & Wilk, M. B. (1965). An analysis of variance test for normality (complete samples). *Biometrika*, *52*(3-4), 591-611.

Shevenell, A. E., Ingalls, A. E., Domack, E. W., & Kelly, C. (2011). Holocene Southern Ocean surface temperature variability west of the Antarctic Peninsula. *Nature*, *470*(7333), 250-254.

Short, M. B., Baygents, J. C., & Goldstein, R. E. (2005). Stalactite growth as a free-boundary problem. *Physics of Fluids (1994-present)*, *17*(8), 083101.

Spliethoff, C. (2015). MSc Thesis Fluid inclusion isotope and calcite analyses of a speleothem from the southern Indian Ocean covering the end of the Younger Dryas.

Stout, J. D., Goh, K. M., & Rafter, T. A. (1981). Chemistry and turnover of naturally occurring resistant organic compounds in soil. *Soil biochemistry*.

Stuart, S. N., Adams, R. J., & Jenkins, M. (1990). *Biodiversity in sub-Saharan Africa and its islands: conservation, management, and sustainable use* (Vol. 6). IUCN.

Tierney, J. E., Russell, J. M., Huang, Y., Damsté, J. S. S., Hopmans, E. C., & Cohen, A. S. (2008). Northern hemisphere controls on tropical southeast African climate during the past 60,000 years. *Science*, *322*(5899), 252-255.

Torrence, C., & Compo, G. P. (1998). A practical guide to wavelet analysis. *Bulletin of the American Meteorological society*, *79*(1), 61-78.

Thompson, L. G., Mosley-Thompson, E., Davis, M. E., Henderson, K. A., Brecher, H. H., Zagorodnov, V. S., ... & Beer, J. (2002). Kilimanjaro ice core records: evidence of Holocene climate change in tropical Africa. *science*, *298*(5593), 589-593.

Troll, C. (1950). Die geographische Landschaft und ihre Erforschung. In *Studium generale* (pp. 163-181). Springer Berlin Heidelberg.

Truc, L., Chevalier, M., Favier, C., Cheddadi, R., Meadows, M. E., Scott, L., ... & Chase, B. M. (2013). Quantification of climate change for the last 20,000 years from Wonderkrater, South Africa: Implications for the long-term dynamics of the Intertropical Convergence Zone. *Palaeogeography, Palaeoclimatology, Palaeoecology*, *386*, 575-587.

Turgeon, S., & Lundberg, J. (2001). Chronology of discontinuities and petrology of speleothems as paleoclimatic indicators of the Klamath Mountains, Southwest Oregon, USA. *Carbonates and Evaporites*, *16*(2), 153.

Winter, K., Holtum, J. A., Edwards, G. E., & O'Leary, M. H. (1982). Effect of low relative humidity on $\delta^{13}C$ value in two C3 grasses and in Panicum milioides, a C3–C4 intermediate species. *Journal of Experimental Botany*, *33*(1), 88-91.

Wolfe, B. B., Aravena, R., Abbott, M. B., Seltzer, G. O., & Gibson, J. J. (2001). Reconstruction of paleohydrology and paleohumidity from oxygen isotope records in the Bolivian Andes. *Palaeogeography, Palaeoclimatology, Palaeoecology*, *176*(1), 177-192.

WWF and IUCN. 1994. Centers of plant diversity. A guide and strategy for their conservation. Volume 1. Europe, Africa, South West Asia and the Middle East. IUCN Publications Unit, Cambridge, United Kingdom.